

# Multicomponent Decompositions for a Sample of S0 galaxies

Eija Laurikainen and Heikki Salo

*Division of Astronomy, Dept. of Physical Sciences, University of Oulu, FIN-90014, Finland*

and

Ronald Buta

*Department of Physics and Astronomy, Box 870324, Univ.of Alabama, Tuscaloosa, AL 35487, USA*

email:eija.laurikainen@oulu.fi

## ABSTRACT

We have estimated the bulge-to-total ( $B/T$ ) light ratios in the  $K_s$ -band for a sample of 24 S0, S0/a and Sa galaxies by applying a 2-dimensional multicomponent decomposition method. For the disk an exponential function is used, the bulges are fitted by a Sérsic's  $R^{1/n}$  function and the bars and ovals are described either by a Sérsic or a Ferrers function. In order to avoid non-physical solutions, preliminary characterization of the structural components is made by inspecting the radial profiles of the orientation parameters and the low azimuthal wavenumber Fourier amplitudes and phases. In order to identify also the inner structures, unsharp masks were created: previously undetected inner spiral arms were found in NGC 1415 and marginally in NGC 3941. Most importantly, we found that S0s have a mean  $\langle B/T \rangle_K$ -ratio of  $0.24 \pm 0.11$ , which is significantly smaller than the mean  $\langle B/T \rangle_R = 0.6$  generally reported in the literature. Also, the surface brightness profiles of the bulges in S0s were found to be more exponential-like than generally assumed, the mean shape parameter of the bulge being  $\langle n \rangle = 2.1 \pm 0.7$ . We did not find examples of barred S0s lacking the disk component, but we found some galaxies (NGC 718, NGC 1452, NGC 4608) having a non-exponential disk in the bar region. To our knowledge our study is the first attempt to apply a multicomponent decomposition method for a moderately sized sample of early type disk galaxies.

## 1 INTRODUCTION

In the present view galaxy evolution has two domains, rapid processes related to hierarchical clustering and merging leading to formation of the main structural components of galaxies (Eggen, Lynden-Bell & Sandage; Toomre 1977; Firmani & Avila-Rees 2003), and slow secular evolution occurring in later phases of galaxy evolution (Kormendy & Kennicutt 2004, hereafter KK04). The slow internal evolutionary processes are assumed to be important for spiral galaxies, but less likely in S0s, where externally induced ram pressure stripping might play a more important role, possibly transforming spiral galaxies into S0s by a loss of gas content (Bekki, Warrick & Yasuhiro 2002).

One of the main reasons to believe that internal secular evolution might be important for spirals, but not for S0s, is the fact that spirals have small exponential bulges or no bulges at all (Carollo et al. 1997; Carollo 1999). As discussed by KK04, the lack of bulges in some spirals probably means that they have not suffered any major mergers during their lifetime. This indicates that in principle there has been enough time for relatively isolated spirals to develop bulges via secular evolutionary processes. On the other hand, S0s are found to have massive bulges (Simien & de Vaucouleurs 1986) with surface brightness profiles similar to those in elliptical galaxies, (Andredakis, Peletier & Balcells 1995, hereafter APB95; Gadotti & de Souza 2003, hereafter GS03), which are easily produced in mergers of two massive disk galaxies (Bekki 1995). However, the properties of S0s are still poorly known. For example, there is recent evidence showing that the bulges in many S0s might be rotationally supported (Erwin, Beckman & Beltran 2004) in a similar manner as the pseudo-bulges in spirals. S0s are also found to be complex systems sometimes having many bars and ovals in the same galaxy (Peng et al. 2002; Erwin et al. 2003), which challenges any simple structural decompositions made for these galaxies.

One of the puzzles for S0s is that they have weak disks, but at the same time also strong bars in many cases. If these galaxies are bulge dominated as generally assumed, it would be difficult to explain the bar formation by a global instability in a cool disk (Binney & Tremaine 1987; Sellwood 2000). However, this paradox is resolved if it is assumed that there is angular momentum exchange between the bar and the spheroidal component: it was shown by Athanassoula (2002, 2003) that in the presence of a massive halo or a large massive bulge, angular momentum is emitted in the inner disk resonances and absorbed in the resonances of the outer disk and halo. In this process an initially weak bar grows stronger and the bar may also consume material that originally belonged to the disk (Athanassoula 2003). In this picture it would be possible to have strong bars even in galaxies dominated by massive bulges. As an extreme case one would see a galaxy with a strong bar, but no sign of the underlying disk, as suggested by GS03.

The above scenario for the formation of bars is an interesting approach to secular evolution of S0s, but there are still

many important observational properties related to this picture that need to be re-investigated: for example, *do most S0s have large massive bulges* as generally assumed and, *do there exist strongly barred S0s without any sign of the disk component?* In this study we measure the bulge-to-total ( $B/T$ ) light ratio for 24 early-type disk galaxies, and analyze in detail NGC 4608, suggested to be a candidate galaxy with a strong bar lacking the disk component (GS03). We use a 2-dimensional multicomponent decomposition method, in which the disk is described by an exponential function, the bulge by a Sérsic's function, and for bars and ovals either a Ferrers or a Sérsic function is used. In order to find physically reasonable solutions the images are first inspected by studying the radial profiles of the orientation parameters, by calculating low azimuthal wavenumber Fourier amplitudes and phases, and by creating unsharp masks.

## 2 THE SAMPLE AND DATA REDUCTIONS

Our sample consists of 24 nearby S0-Sa galaxies ( $-3 < T < 1$ ) having total magnitudes  $B_T < 12.5$  mag and inclinations less than  $65^\circ$ . This is part of our Near-IR S0 Survey (NIRS0S) of 170 S0-Sa galaxies selected to be comparable in size, total apparent magnitude, and number with the Ohio State University Bright Galaxy Survey (OSUBGS, Eskridge et al. 2002) for spirals, for which we have previously made similar analysis as presented in this study (Buta, Laurikainen, Salo 2004; Laurikainen, Salo, Buta 2004; Laurikainen et al. 2004, hereafter LSBV04). The galaxies are mainly S0s, but some early-type spirals are included to ensure a small overlap with the OSU sample, and also because galaxies tend to look earlier in the near-IR than in the optical. The subsample of 24 galaxies was selected to have a large variety of bar and bulge sizes. The sample is listed in Table 1, where the morphological types are from the Third Reference Catalog of Bright Galaxies (de Vaucouleurs et al. 1991, RC3). Some of the galaxies have active nuclei, the activity types being taken from the NASA/IPAC Extragalactic Database (NED).

We present high resolution  $K_s$  and  $B$ -band observations carried out at the 2.5 m Nordic Optical telescope (NOT) in La Palma in Jan 2003 and Jan 2004. The observations were made in good weather conditions. Full Width at Half Maximum (FWHM) values for the point spread function were measured using several foreground stars and are listed in Table 1. The average value is 1.1 arcsec. The  $K_s$ -band observations were obtained using NOTCam, a 1024 x 1024 detector array with a pixel size of 0.23 arcsec pixel $^{-1}$  and a field of view of 4 x 4 arcmin $^2$ . The total on-source integration time was generally 1800 sec and the integration time in one position was taken in snapshots of 20-30 sec. Owing to the high sky brightness in the near-IR, the sky fields were taken in two directions to avoid bright foreground stars and alternating between the galaxy and the sky field in periods of one minute. In order to avoid interference patterns and hot pixels in the images, dithering of 5 arcsec was used in the galaxy field and a larger dithering was used in the sky field. Twilight flats only were used and were

constructed by subtracting a low ADU-level image from a high ADU-level image.

All images were processed using the IRAF package routines<sup>1</sup>. The reduction steps consisted of sky subtraction, combining the on-source integrations, flat-fielding, cleaning the images, and transposing the images to have North up and West on the right. Generally the best sky subtraction was achieved using the temporally nearest sky frame for each science frame. Pickup noise in some of the images was removed using a destriping method described by Buta & McCall (1999). Images were cleaned of foreground stars using DAOFIND to find the stars initially. Then a combination of point spread function (PSF) fitting and image editing (IMEDIT) was used to remove the stars.

Optical *B*-band observations were obtained using the 2048 x 2048 ALFOSC CCD, which has a field of view of 6.5 x 6.5 arcmin<sup>2</sup> and a pixel size of 0.19 arcsec pixel<sup>-1</sup>. For the high surface brightness centers of many S0s, the integrations were generally divided in a number of short exposures so that the total integration time was 1800 sec. As the CCD field was always larger than the galaxy size, no extra sky fields were obtained. Twilight flats were used, and the standard reduction steps (combining the images, bias subtraction, flat-fielding, cleaning and transposing the images) were performed using the IRAF routines. For the galaxies with both optical and near-IR observations, the relative difference in the direction of the North in the sky plane was checked between the *B* and *K<sub>s</sub>*-band images using the IRAF routine GEOMAP.

### 3 IDENTIFICATION OF THE STRUCTURAL COMPONENTS

S0 galaxies generally have complicated morphological structures, which challenges the determination of their bulge-to-total (*B/T*) light ratios. Besides bulges and disks, S0s may also have bars, inner disks and ovals, which are not always visible in the azimuthally averaged surface brightness profiles: if a component in question has a low surface brightness compared to the surface brightness of the bulge, it is easily overshadowed by the bulge. Before any reliable decompositions can be made, a *priori* evaluation of the existence of these components is required. As we take the approach that bulges in S0s can be either classical bulges with the  $R^{1/4}$ -law type profiles or pseudo-bulges, the concept of a bulge is not self-evident. For example there are views according to which pseudo-bulges are actually evolved bars seen edge-on (Athanasoula 2002, 2005): when the bar is created it is thin, and when it evolves in time its vertical extent increases particularly in the inner part of the bar and the morphology turns to a boxy or peanut-shaped structure. It has also been shown by Samland & Gerhard (2003) that bulges formed at different times may appear in the same galaxy.

<sup>1</sup> IRAF is distributed by the National Optical Astronomy Observatories, which are operated by the Association of Universities for Research in Astronomy, under cooperative agreement with the National Science Foundation

In spite of this phenomenological problem, some rules of thumb can be used to identify the different components. We particularly follow KK04, who define a *pseudo-bulge* as a nearly exponential structure ( $n = 1-2$ ), which in some cases might have a boxy/peanut shaped structure and particularly, its flattening is similar to that of the outer disk. *Lenses* (or ovals in spirals) might have similar ellipticities as pseudo-bulges (typically  $b/a > 0.85$ ), but in distinction to pseudo-bulges, they generally have lower surface brightnesses and rather sharp outer edges (KK04). *Inner disks* can be clearly identified, if the galaxy has near-nuclear spiral arms. In unclear cases the elliptical inner structure is assumed to be an inner disk if its position angle  $\phi$  differs from  $\phi$  of the outer disk by less than  $10^\circ$  (see Erwin & Sparke 2003, hereafter ES03). In order to identify the different components we measure (1) *the radial profiles of the ellipticities and position angles*, (2) *the radial profiles of the low azimuthal wavenumber Fourier amplitudes and phases*, and construct (3) *unsharp masks*. Bars, lenses and inner disks all appear as bumps in the ellipticity profiles, if their surface brightnesses are high compared to that of the underlying disk. The Fourier method is sensitive for detecting weak bars and ovals, whereas the unsharp masks are capable of showing also the innermost structures of galaxies.

### 3.1 The orientation parameters

*B*-band images were used to measure the radial profiles of the isophotal major-axis position angles ( $\phi$ ) and the minor-to-major axis ratios ( $q = b/a$ ). The position angles and inclinations of the disk were estimated from the mean values in the outer parts of the disks. If no *B*-band images were available the orientation parameters were estimated using *K<sub>s</sub>*-band images: these images were first compared with the Digitized Sky Survey plates to ensure that the outer parts of the disks are visible. The surface brightness profiles and the orientation parameters were derived using the ELLIPSE routine in IRAF (Jedrzejewski 1987): a linear radial scaling in steps of one pixel was used to have good spatial resolution particularly in the outer parts of the disks. In order to minimize the effects of noise and contamination by bad pixels and cosmic rays, deviant pixels above  $3\sigma$  were rejected. The measured disk position angles and axial ratios are shown in Table 2, where the uncertainties are standard deviations of the mean calculated in the radial range indicated in the table. The outer disk of NGC 2781 is so weak that the ELLIPSE routine failed. In this case the orientation parameters were determined manually by adjusting an ellipse to the outer isophotes. For comparison, the table also shows the orientation parameters given in RC3 and those obtained by ES03. The  $q$  and  $\phi$  profiles are shown in Fig. 5 with a logarithmic radial scale, in order to better illustrate the presence of the different structural components.

The orientation parameters found in this study are generally in good agreement with those obtained by ES03, who used high resolution *R*-band images for their measurements. We have 9 galaxies in common with their sample and good agreement

was found for 7 of the galaxies. However, for NGC 2859 we measure a considerably smaller  $q$ -value (0.76 vs. 0.90): it seems that the image used by ES03 ends up to the outer ring, while we measure also the extended disk outside the ring thus giving a more reliable estimation of  $q$ . Also, the position angles of NGC 1022 and NGC 2681 are completely different in the two studies, but this is not very surprising taking into account that these galaxies have almost circular outermost isophotes. While comparing the measured orientation parameters with those given in RC3 larger deviations were found, which is expected because RC3 orientation parameters are based on photographic plates, which do not have the same depth and quality as the modern CCD images.

### 3.2 Fourier decomposition and unsharp masking

Fourier decompositions are calculated from the  $K_s$ -band images in different radial zones and the amplitude and phase of each component is tabulated as a function of radius (Salo et al. 1999; LSBV04). The Fourier modes up to  $m = 10$  were calculated, although the main modes in bars and ovals are  $m = 2$  and  $m = 4$ . Bars are identified mainly by assuming that the phases of the  $m = 2$  and  $m = 4$  amplitudes are maintained nearly constant in the bar region, in distinction to spiral arms, where the phase changes as a function of radius. Another useful way of identifying bars is to map the galaxy image into a log polar coordinate system: a bar appears in the image either as a linear structure or as a bright spot, depending on the radial surface brightness profile of the bar. A contrast between the bar and the surrounding region can be highlighted by subtracting the  $m = 0$  component from the image. The polar angle maps as well as the amplitudes and phases of the  $m = 2$  and  $m = 4$  Fourier modes are shown for all 24 galaxies in Fig. 1. Before calculating the Fourier modes, the images were deprojected to face-on orientation using the method described in LSBV04: we use a 2D decomposition method to estimate the relative flux of the bulge component, which is subtracted from the original image. In these decompositions a bulge model with circular isophotes is used. The image is then deprojected to face-on orientation after which the bulge is added back by assuming that it has a spherical 3D light distribution. This deprojection method was preferred in order to avoid artificial stretching of nearly spherical bulges while deprojecting 2-dimensional images. As bulges in some galaxies are not circular, this might also be the reason for the large  $A_m/A_0$ -ratio at the very center in some of the galaxies in Fig.1. Notice that in the decompositions shown in Section 4 the bulges are not restricted to have circular isophotes.

An unsharp mask works as a filter suppressing large-scale low-frequency variations in the images (Malin & Zealey 1979; ES03). In this study a mask was created by making a smoothed copy of the original  $K_s$ -band image, which was then subtracted from the original image. Typical windows used for smoothing the images varied between 5 to 20 pixels, depending on the size of the inner structure of the galaxy. In principle it is also possible to divide the original image with the smoothed image,

but that was only occasionally done. Due to increased contrast between the non-axisymmetric structure and the surrounding region, it is possible to better estimate the inner morphology of the galaxies, for example by distinguishing secondary bars from inner rings and inner spiral arms, which all appear in a similar manner in the  $q$ -profile. The unsharp masks are shown in Fig. 5.

### 3.3 Discussion of individual galaxies

The identified structural components are listed in Table 3, where the primary bars are denoted as  $bar_1$ , the secondary bars as  $bar_2$ , and the tertiary bars as  $bar_3$ , and if only one bar appeared in a galaxy, simply as  $bar$ . In case of three bars, as in NGC 2681,  $bar_2$  is the most prominent bar in the galaxy and  $bar_3$  denotes the extremely faint bar at a larger radius. Following KK04, if a galaxy has a morphological type of S0 - S0/a the flat inner structure is called a *lens* and for later morphological types it is called an *oval*. The number in parentheses indicates the semi-major axis length of the structure in arcseconds. This length has been estimated from the phases of the  $m=2$  Fourier modes which give systematically slightly longer bars than estimated from the minima in the  $q$ -profiles (Laurikainen & Salo 2002). Below we discuss observational evidence for these components for most galaxies. As discussed above, the original images appear in Fig. 4 (upper left panel), the Fourier amplitudes and phases in Fig. 1, and the unsharp masks and the radial profiles of the orientation parameters in Fig. 5.

**NGC 718:** This galaxy has a primary bar extending to  $r = 20$  arcsec and also shows weak evidence of a secondary bar at  $r = 5$  arcsec (Figs. 1 and 5), previously detected in the  $R$ -band by ES03 as an elliptical inner component. Both structures appear as minima in the  $q$ -profile and in the case of the primary bar, also as a rapid change in the position angle at the end of the bar. Both features have significant peaks in the  $m = 2$  and  $m = 4$  amplitudes of density. For the primary bar the  $m = 2$  and  $m = 4$  phases are also maintained nearly constant in the bar region, and in the polar angle map the bar is identified as an intensity maximum at  $r = 20$  arcsec. The weak innermost structure can be detected also in the polar angle map and marginally in the unsharp mask.

**NGC 936:** Characteristic for this galaxy is a prominent bar, an oval and a small nearly spherical bulge. In the central part of the galaxy there is also a small elliptical structure (Fig. 5), which was identified as a nuclear ring by ES03 in a high resolution (0.11 arcsec)  $R$ -band image. The bar and the inner elliptical structure are both identified in the Fourier analysis, and the primary bar also as a minimum in the radial  $q$ -profile.

**NGC 1022:** NGC 1022 is a peculiar dusty ringed galaxy discussed also by ES03. It is classified as a barred galaxy both in RC3 and by ES03, but our Fourier analysis shows that the phase of the  $m = 2$  amplitude is not maintained constant in the assumed bar region, indicating a spiral-like nature of this structure, seen also in the polar angle map. Other similar cases

among spiral galaxies have been earlier discussed by LSBV04. This galaxy has also a slightly flattened oval inside the bar, and a pseudo-ring surrounding the bar-like structure.

**NGC 1415:** This galaxy is classified as having an intermediate type bar in RC3, and it is also reported to have an elliptical inner structure in the red continuum by Garcia-Barreto & Moreno (2000) and in the 2MASS images by Erwin (2004). Garcia-Barreto & Moreno interpreted it as a secondary bar, but due to the similarity in position angle with the main disk, Erwin suggested that it might be an inner disk. We found near nuclear spiral arms at  $r = 9$  arcsec, being well illustrated in the unsharp mask (Fig. 5) and visible also in the polar angle map, which confirms the disk-like nature of this structure. The primary bar has ansae at the two ends of the assumed bar, but the morphology has some disk-like characteristics. Our  $K_s$ -band image is not very deep, showing only the bar region but not the outer exponential disk.

**NGC 1440:** This galaxy has a classical bar detected by all our criteria. There is also a large lens inside the bar and a small, almost spherical bulge.

**NGC 1452 :** NGC 1452 is a barred galaxy having a prominent ring around the ends of the bar, a large oval inside the bar, and a small bulge.

**NGC 2196:** This is a non-barred galaxy, but has an elliptical inner structure, which is not completely aligned with the underlying disk. The inner elliptical structure appears also as a strong  $m = 2$  peak in the amplitude profile in the Fourier analysis.

**NGC 2273:** This is a famous barred galaxy with four rings (see e.g. discussion in Buta & Combes 1996), studied previously by ES03 in the optical and using NICMOS HST images. They showed that, besides the bar, this galaxy has also nuclear spiral arms inside a nuclear ring. We confirm the presence of the near nuclear spirals in our ground-based infrared image at  $r = 2-3$  arcsec (Fig. 5), and these arms are clearly visible also in the polar angle map. The bar is well detectable in the polar angle map, but the  $m = 2$  phase is maintained nearly constant at a much larger radius from the galaxy center than the bar region alone, mainly because this galaxy has rather open spiral arms outside the bar. The inner disk is surrounded by an oval or a flattened bulge.

**NGC 2460:** This galaxy is classified as a non-barred galaxy in RC3, but clearly has an elongated inner structure at  $r < 10$  arcsec, detected as a bar-like structure in the  $q$  and  $\phi$ -profiles and in the Fourier analysis. As the position angle of this structure deviates even by  $25^\circ$  from that of the main disk, it might be a weak secondary bar.

**NGC 2681:** NGC 2681 has been found to be a triple barred galaxy by ES03 and by Erwin & Sparke (1999), based on both ground-based and HST NICMOS images. All three bars are detected also in this study, as minima in the  $q$ -profile and



as blobs in the polar angle map. This galaxy also has a nearly round lens at the radius of the secondary bar.

**NGC 2781:** NGC 2781 is classified as a weakly barred galaxy in RC3. Characteristic for this galaxy is an extremely faint outer disk and elliptical structures at the distances of  $r < 45$  arcsec and  $r < 10$  arcsec from the galaxy center. Both elliptical structures are visible as minima in the  $q$ -profile and as intensity maxima in the Fourier analysis. The unsharp mask (Fig. 5) shows that the smaller structure is actually an inner disk with a two-armed spiral. The outer elliptical is most probably a bar, but does not have the typical rectangular shape of a classical bar, usually associated with a small axial ratio (in this case  $q = 0.52$ ). Both the inner and outer elliptical structures deviate  $15^\circ$  from the orientation of the outer disk.

**NGC 2859:** In the optical this galaxy is classified as a double barred galaxy (Kormendy 1979; Wozniak et al. 1995), having also inner and outer rings (RC3). We confirm the double barred nature in the near-IR, which is obvious using all our criteria for bars. In the unsharp mask the secondary bar has a rectangular morphology typical for a classical bar. This galaxy has also two ovals, one at the radius of the primary bar, and another inside that bar.

**NGC 2911:** NGC 2911 clearly has no bar/oval components, only a disk and a slightly flattened bulge. However, it has a peculiar inner structure with a tiny polar edge-on disk in the very center (Sil'chenko & Afanasiev 2004).

**NGC 2983:** This galaxy has a strong bar, a central elliptical structure, and a lens inside the bar. The primary bar is well visible in the  $q$ -profile and in the Fourier analysis, whereas the inner elliptical appears only as a density peak in the  $m = 2$  amplitude profile. The secondary bar can be identified also in the unsharp mask (Fig. 5). The primary bar has an ansae-type morphology with blobs at the two ends of the bar.

**NGC 3414:** This is a peculiar galaxy, which looks like a barred system with a large oval, but different interpretations have been given of its true nature. For example, Whitmore et al. (1990) suggested that it is a galaxy seen edge-on with a large-scale polar ring in the  $R$ -band, whereas according to BBA98 and Chitre & Jog (2002) it might be a nearly face-on galaxy with a prominent bar.

**NGC 3626:** In RC3 this galaxy is classified as a non-barred system with an outer ring. However, both the  $q$ -profile and the Fourier analysis show the presence of a bar at  $r < 45$  arcsec, having a morphology with ansae at the two ends of the bar (Fig. 5). This galaxy has also an inner elliptical, detected as a bar-like structure at  $r = 5$  arcsec by the Fourier analysis, and as an elliptical feature in the unsharp mask. The position angle of this structure deviates from that of the main disk by  $10^\circ$ , and might actually be an inner disk.

**NGC 3941:** This galaxy is classified as a double barred system by ES03 in the optical region. In the  $K_s$ -image the main bar has ansae-type morphology and all characteristics of a bar. However, the unsharp mask shows that the inner elliptical is

rather an inner disk showing two-armed spirals (Fig. 5). Both the inner disk and the bar appear as minima in the  $q$ -profile and are identified as intensity peaks in the Fourier analysis. This galaxy has also an oval inside the bar.

**NGC 4245:** In RC3 this galaxy is classified as a barred galaxy with an inner ring. ES03 found a nuclear ring in  $R$ -band, but no evidence of a secondary bar in the optical HST image. ES03 also report dust lanes in the inner ring leading into a nuclear spiral that continues into the nucleus. The nuclear ring at  $r = 5$  arcsec is visible also in our unsharp mask of the  $K_s$ -band image (Fig. 5). NGC 4245 has an oval surrounding the secondary bar.

**NGC 4340:** In the optical region this galaxy has been classified as a double barred system by Erwin (2004), the secondary bar being surrounded by a nuclear ring. Both bars are identified also in our  $K_s$ -band image, by all indicators of a bar. The secondary bar is aligned with the primary bar, which deviates from that of the underlying disk. This galaxy has also a nearly spherical bulge and an oval inside the primary bar.

**NGC 4608:** This galaxy is classified as a barred system with an inner ring in RC3. Both components are visible also in our  $K_s$ -band image. Additionally, NGC 4608 has a large oval inside the bar, and apparently a small spherical bulge. This galaxy has been reported as a candidate of barred galaxies without any sign of the disk component (GS03) and will be discussed in detail in Section 4.

**NGC 4643:** This is a famous barred Polar Ring galaxy (Whitmore et al. 1990), studied previously also by ES03. They found an elliptical inner structure in the optical region, and based on an unpublished high resolution  $H$ -band image by Knapen that structure was interpreted to be an inner ring. Our  $K_s$ -band image shows four knots in the central part of the galaxy, which most probably indicates the presence of a nuclear ring (Fig. 5).

#### 4 MULTICOMPONENT 2D-DECOMPOSITIONS

For structural decomposition of galaxies, three main types of methods have been generally used: (1) one-dimensional (1D) methods, where either a major axis surface brightness cut or an azimuthally averaged profile is fitted by assuming various functions for the bulge and the disk, (2) the Kent (1985) method where the bulge and the disk are separated based on their different isophotal ellipticities, and (3) two-dimensional (2D) methods, where the model functions for the bulge and the disk are fitted simultaneously to all pixels of the image. The advantage of using azimuthally averaged profiles and a 1D method is the small amount of noise in the profile, whereas Kent's method is powerful in separating the bulge without any specific assumptions of the functional form of the bulge or disk. However, for galaxies with strong non-axisymmetric structures like bars both methods might fail, because omitting a large bar in the decomposition might overestimate the light attributed to the bulge model (LSBV04; see also discussion in Section 4.2).

The first 2D methods used the de Vaucouleurs's  $R^{1/4}$  law for the bulge (Byun & Freeman 1995; Shaw & Gilmore 1989; de Jong 1996; Wadadekar, Robbason & Kembavi 1999), but later studies have shown that the more general Sérsic's  $R^{1/n}$  function (Sersic 1968) can better account for the bulge profiles. This has been shown for the bulges of late to intermediate type spirals (Möllenhoff & Heidt 2001; Simard et al. 2002; MacArthur, Courteau & Holtzman 2003), and also for the bulges of S0s (D'Onofrio, Capaccioli & Caon 1994; de Souza, Gadotti & dos Anjos 2004) and even for the surface brightness profiles of elliptical galaxies (Caon, Capaccioli & D'Onofrio 1993).

In spite of the fact that the 2D method is a powerful tool for separating non-axisymmetric structures in galaxies, that advantage has been only occasionally used (de Jong 1996; Prieto et al. 2001; Peng et al. 2002; LSBV04). In the following our method together with some tests will be briefly described, and its application for the galaxies in our sample are discussed.

#### 4.1 The algorithm

We use a 2D decomposition method where, in addition to a bulge and a disk, up to three non-axisymmetric structures can be simultaneously fitted. For the radial profile of the bulge we use a Sérsic function, while the disk is always assumed to be exponential; for the bar-like structures either a Ferrers or a Sérsic function is used. No inner truncation is used for these components. An exponential inner disk and a nuclear Gaussian point source can also be included, so that the maximal number of fitted components is seven (the maximal number of free parameters is 31). Due to practical reasons related to computing time and difficulties caused by the possible degeneracy between the fitted components, this seems like a reasonable upper limit. Also, the method is flexible in the sense that the user can decide which of the model parameters are fixed and which are free variables in the fit; also any number of the components can be omitted from the fit.

The fitting is performed in flux-units, which makes it possible to take into account also the faint outer regions of the images, where some fraction of the pixels have negative values. The best solution is found iteratively, where fitting to the data is accomplished by minimizing the weighted squared deviations of the data from the fit:

$$\chi^2 = \sum_i^{N_{pix}} w_i (F_i - F_{model})^2, \quad (1)$$

where  $F_i$  and  $F_{model}$  denote the measured and modeled surface brightnesses at each image pixel,  $i = 1, \dots, N_{pix}$ , and  $w_i$  is the weight assigned to each pixel. The minimization of the deviations between the original image and the model is made with the IDL procedure CURVEFIT.

Depending on the choice of the weighting function, more weight can be assigned to the pixels in the central parts of the galaxy where the surface brightness is high, or it can be used to emphasize the faint outer disk. One natural choice would be

to use a weight related to the distribution of noise in the image:  $w_i = 1/\sigma_i^2$ , where  $\sigma_i$  denotes the standard deviation of  $F_i$ . In the case of Poisson noise this would imply  $w_i = 1/F_i$ . The effects of the weighting function in the decompositions will be discussed in the next section. In order to account for the effects of *seeing*, the model is convolved with a Gaussian PSF using a FWHM measured for each observed image. No attempt was made to correct the effects of dust, but the problem is not very serious in the near-IR, where the extinction is minimal, and particularly it is not serious for early-type galaxies that generally have only a small amount of dust.

All components (including the bulge) are allowed to follow a generalized elliptical shape (Athanasoula et al. 1990), defined by the equation:

$$r = (|x|^{c+2} + |y/q|^{c+2})^{1/(c+2)}. \quad (2)$$

The shape of the isophote corresponding to  $r = \text{constant}$  is boxy when the shape parameter  $c > 0$ , diskly when  $c < 0$ , and purely elliptical when  $c = 0$ ; circular isophotes correspond to  $c = 0$  and an axial ratio  $q = 1$ . Here  $x$  and  $y$  are the rectangular coordinates in a system aligned with the major axis of the component in question, defined by its position angle  $\phi$ .

A Sérsic's function is used to describe the brightness profile of the bulge:

$$I_b(r_b) = I_{0b} \exp[-(r_b/h_b)^\beta], \quad (3)$$

where  $I_{0b}$  is the central surface density,  $h_b$  is the scale parameter of the bulge, and  $\beta = 1/n$  determines the slope of the projected surface brightness distribution of the bulge. The coordinate  $r_b$  is the isophotal radius defined by Eq. 2, using the parameters  $q_b$ ,  $c_b$  and  $\phi_b$ , where the subscript stands for the bulge. In the case of an elliptical bulge,  $\phi_b$  is its major axis position angle measured counter clockwise from North in the sky plane. Special cases of Sérsic's formula are the exponential function with  $n = 1$  and the de Vaucouleurs  $r^{1/4}$  law with  $n = 4$ . Note that since the numerical value of  $h_b$  depends strongly on  $\beta$ , we typically describe our fitted bulge models with the bulge effective radius  $r_{eff}$  (radius of the isophote that encompasses half of the total bulge light).

Bars (and ovals/lenses) are fitted using a function, which has the form:

$$\begin{aligned} I_{bar}(r_{bar}) &= I_{0bar} (1 - (r_{bar}/a_{bar})^2)^{n_{bar}+0.5}, \quad r_{bar} < a_{bar} \\ &= 0, \quad r_{bar} > a_{bar}, \end{aligned} \quad (4)$$

where  $I_{0bar}$  is the central surface brightness of the bar,  $a_{bar}$  is the bar major axis, and  $n_{bar}$  is the exponent of the bar model defining the shape of the bar radial profile. The isophotal radius ( $r_{bar}$ ) is defined via parameters  $q_{bar}$ ,  $c_{bar}$ ,  $\phi_{bar}$  in Eq. 2.

For bar components we have two choices for the reference plane: besides the sky plane one can also specify the bar shape and orientation parameters using the disk plane as a reference plane, in which case  $\phi_{bar}$  is counted counter clockwise along the disk plane from its nodal line. The function (Eq. 4) corresponds to a projected surface density of a three dimensional prolate Ferrers bar, with  $a > b = c$ , seen along the  $c$ -axis. Thus the possible 3D structure of a bar is not taken into account. Alternatively, the radial profiles of bars (and ovals/lenses) can be described by a Sérsic's function. The advantage of using a projected Ferrers function is that it is rather flat and that the surface brightness drops near the outer edge, as is the case also for bars and ovals in real galaxies. Taking into account that bars typically have rectangular shapes, more realistic bar models are obtained if the shape parameter  $c_{bar}$  is also added. The Ferrers function is expected to work well especially for bars in early-type galaxies, which are known to have flat surface brightness profiles (Elmegreen & Elmegreen 1985). But for some galaxies a Sérsic's function with a more centrally peaked profile might also give reasonable fits. Disk components are described with an exponential function

$$I_d(r) = I_{0d} \exp[-(r/h_r)], \quad (5)$$

where  $I_{0d}$  is the central surface density of the disk, and  $h_r$  is the radial scalelength of the disk. For the disk the radius  $r$  is always calculated along the disk plane, defined by the position angle  $\phi_d$  and axial ratio of the disk  $q_d$ . In principle,  $\phi_d$  and  $q_d$  can also be free variables in the fit; however, in the current study they are fixed to the values derived from observations like those described in section 3.1. Inner disks can be fitted by an exponential function, and as for bars the vertical thickness of the disk component is ignored. In principle, active nuclei and other bright central sources can be fitted with a Gaussian PSF, but that is not done in this study.

A three-component version (bulge/disk/bar) of this algorithm has been previously used in the studies by LSBV04, Laurikainen, Salo & Buta (2004) and by Buta, Laurikainen & Salo (2004).

## 4.2 Testing the method

The decomposition method was tested by applying it to synthetic images, created using a Sérsic's function for the bulge, and an exponential function for the disk, and in some cases also a Ferrers' function for the bar. In order to have realistic images Poisson noise and background noise were added, and the images were convolved with a Gaussian PSF,  $\sigma_{PSF}$  (=FWHM/2.355) imitating the typical *seeing* in the science images. A typical inclination of the disk ( $30^\circ$ ) was also assumed. If not otherwise mentioned the resolution in the test images was taken to be similar to that in the original science images. Decompositions for the test images were performed starting from initial parameter values that deviated significantly from the true parameters of the created images.

The effect of the weighting function on the scalelength of the disk was investigated for a synthetic galaxy image with  $\beta = 0.5$  ( $n = 2$ ) and bulge-to-disk ratio  $B/D = 0.2$ . The bulge effective radius  $r_{eff} = 3$  and the disk scalelength  $h_r = 30$  pixels. The amount of noise was specified by setting the signal-to-noise ratio  $S/N = 3.0$  at the distance of  $4h_r$  (separately for the Poisson and the background noise component, so that the total  $S/N$  is in fact  $\sqrt{2}$  times smaller). Another case with twice larger noise level ( $S/N = 1.5$ ) was also examined, representing an already very noisy image. A *seeing* with  $\sigma_{PSF} = 1$  was added. The results for different weighting functions are given for two different  $S/N$ -ratio in Tables 4a and 4b, using a large range of possible  $r$  and  $F$  combinations, where  $r$  denotes the pixel distance from the center along the disk plane and  $F$  is the corresponding flux: note the difference between  $F$  and  $F_{model}$  in the table, the former being the observed pixel value while the latter is the corresponding model value for this pixel. In the case the pixel flux  $F$  was below a  $3\sigma$  noise level it was replaced with this value when used in a weighting function. The rows in this table are ordered according to an increasing relative weight given to the outer parts of the galaxy (i.e.  $w = 1/r^2$  weights very strongly the inner galaxy while  $w = r/F_{model}$  places more weight on the outer disk).

We found that the decomposition works well in this simple bulge/disk case, regardless of the exact choice of the weighting function. For the images with high S/N-ratio poor results are obtained only for the function  $w = 1/r^2$ , giving more weight to the inner pixels: it tends to underestimate the scalelength of the disk and gives large deviations from the true shape parameters of the bulge. Besides  $h_r$ , these weighting functions also give nearly correct effective radii for the bulge component, within an accuracy of 0.2%. Also, the  $B/D$ -ratio is independent of the weighting function used. For noisy images poor results are generally obtained when weighting functions based on the observed  $F$  were used. But even in this case the results are fairly accurate for weighting functions like  $w = 1/(F_{model}r)$ ,  $w = r$ , or  $w = 1/F_{model}$ . In this case the results with  $w = r/(F_{model})$  also become sensitive to the starting values of the iteration, indicated by the empty bin in the table. The behavior of the weighting functions involving the observed fluxes  $F$  is also fairly interesting: particularly in the case of larger noise it is evident that fits with these weighting functions tend to converge to values of  $h_r$  which are *systematically* too low. The above tests show that neither the  $B/T$ -ratio nor the parameter  $\beta$  of the bulge are sensitive to the weighting function used: the decomposition becomes sensitive to the weighting function only if the image is very noisy, or as will be discussed later, if complicated galaxy morphology is fitted by a simple decomposition model.

Next the effect of *seeing* on the parameters of the bulge was investigated. We first checked that the original parameters of the synthetic images, smeared by *seeing*, are very accurately recovered when the correct  $\sigma_{PSF}$  is used in convolving the model functions. On the other hand, if the *seeing* correction is not included in the fit, or an inaccurate *seeing* correction is

applied, substantial errors in the derived bulge parameters are possible. Table 5 collects some results, using synthetic images that contained only a bulge component, with  $\beta = 0.25, 0.50,$  and  $1.0$ , thus ranging from de Vaucouleurs's type bulge ( $n = 4$ ) to an exponential bulge with  $n = 1$ . No noise is added, and in order to assure that the pixel resolution does not cause problems, a large effective radius of  $r_{eff} = 20$  pixels is used. According to this table, the case of a poor *seeing* combined with a compact bulge can lead to a serious under or overestimate of  $\beta$  if the *seeing* in the image is not well determined. If no *seeing* correction is made the effect of *seeing* is to make the bulge more exponential than it actually is: as an extreme case, a de Vaucouleurs type profile ( $n = 4$ ) appears as an exponential bulge ( $n = 1$ ).

As one of the key issues in this study is to apply multicomponent decomposition to galaxies with prominent bars and ovals, we also checked *how much omission of the bar in the decomposition may affect the B/T-ratio*. Synthetic test images were created (1) having only a bulge and a disk, and (2) then adding a large bar to that galaxy model. A Ferrers function for the bar was used, the bulge parameters were taken to be  $\beta = 0.60$  and  $h_b = 1.0$ , and the scalelength of the disk  $h_r = 45$ . Again, in order to create realistic images, *seeing* and noise were added to the synthetic data, comparable to those used in the tests in Table 4. The decompositions for these two synthetic images are shown in Fig. 2.

As expected, applying a bulge/disk decomposition to the first test image recovers the bulge and the disk parameters with relatively high accuracy (Fig. 2a). Particularly, we found  $B/D = 0.38$ , in comparison to the input  $B/D = 0.37$  in the synthetic image. For the second test image two types of decompositions were made, namely bulge/disk (Fig. 2b) and bulge/disk/bar decompositions (Fig. 2c), both giving relatively good looking fits for the surface brightness profile. We found that when fitting all three components, the correct  $B/D = 0.37$  was returned. However, if only a bulge and a disk were fitted,  $B/D = 0.57$  was obtained, which overestimates the  $B/D$ -ratio even by  $1/3$ . It is evident that in the bulge/disk decomposition a significant fraction of the bar flux was erroneously assigned to the bulge, illustrated in the residual image where both positive and negative pixel values are visible. The negative residuals appear due to the fact that too much light is subtracted in a region slightly exceeding the radius of the bar, whereas the positive residuals appear because the bar itself was only partially subtracted.

As the above galaxy model has a small  $B/D$ -ratio with a small spherical bulge, other models with higher  $B/D$ -ratios were also studied (see Table 6). Three galaxy models were created with  $B/D$ -ratio near unity: in *model 1* the bulge was taken to have  $\beta = 0.5$ , whereas in *model 3*  $\beta = 0.33$ . One of the models (*model 2*) also tested the effect of a non-spherical shape of the bulge ( $q = 0.9$ ) in the decomposition. All galaxy models also included a prominent bar modeled by a Ferrers function with  $n_{bar} = 2$  and an ellipticity  $q = 0.3$ . This bar contributed to the total flux by  $(\text{bar light})/(\text{total light}) = 0.1$ . As above, also in

this case *seeing* and a small amount of noise were added to the images. The created images were fitted either by bulge/disk or bulge/disk/bar decomposition. In order to simultaneously test also the effect of the weighting function, all test images were decomposed with three different weighting functions:  $w_i$  proportional to  $1/F_i$  or  $r_i$ , or the same weight was used for all pixels. We found that when all three components were fitted simultaneously the true  $B/D$  and  $\beta$ -values were recovered with a high accuracy for all three models. The solutions were also practically independent of the weighting function used. However, if only a bulge and a disk were fitted large deviations from the true  $B/D$  and  $\beta$ -values appeared (the deviations from the true values are indicated in parenthesis). In this case also the weighting function started to be important: for example using a constant weight for all pixels in the image, *model 3* gave a solution where the whole profile could be fitted nearly by one single function. While comparing the two models which deviated only by the ellipticity of the bulge (*models 1* and *2*), similar results were obtained. Based on the above tests it seems that by omitting a prominent bar in the decomposition systematically overestimates the  $B/T$ -ratio, assigning a significant fraction of the bar flux to the flux of the bulge.

S0 galaxies generally have weak disks and therefore it is important to study *the limiting cases where the disk might be erroneously lost* in the decomposition, for example because they are overshadowed by luminous bulges or because the disks are too noisy. An example of a galaxy model with a massive rather exponential-like bulge, but having a nearly  $R^{1/4}$  law type total surface brightness profile is shown Fig. 3a: in this model the bulge has  $\beta = 0.5$  (or  $n = 2.0$ ), the disk has  $h_r = 50$ , and  $B/D = 1.4$ . Also, the image is truncated already at 100 pixels, or two disk radial scalelengths. In spite of the lack of a visually detectable exponential part in the surface brightness profile our method still finds the scalelength of the disk with a high accuracy ( $h_r = 51$ ). If a similar profile is created, but using  $\beta=0.3$  (or  $n = 3.3$ ) and higher noise level is added, it is possible to miss the disk, but only if completely erroneous initial parameters are given for the bulge (Fig. 3b). In this case the disk is lost suddenly after several iterations, but the final model is far from the surface brightness profile of the created image, showing that a single function is not capable of accounting for this profile. Finally, Figs. 3c-d show tests using a galaxy model having a weak and noisy disk dominating the outer part of the galaxy, and a rather small bulge with a nearly de Vaucouleurs's type surface brightness profile ( $\beta = 0.3$ ). The two decompositions shown for this model are otherwise similar, except that different weighting functions are used. We found that while it is not possible to miss the disk in these decompositions, a bad choice of the weighting function can lead to considerable errors in the fitted disk scalelength: in Fig. 3d we used the instrumental Poisson weighting  $w = 1/|F|$ , without any lower noise limit (the absolute value was taken to avoid negative weights), whereas in Fig. 3c  $w = r$ . Incidentally, these test images resemble the galaxy NGC 2911 in our sample. It appeared that the disk was properly found using  $w = r$ , but not when the weight is proportional to  $1/F$ . However,  $w = 1/F_{model}$  recovers the correct



parameters with the same accuracy as the weight  $w = r$ .

### 4.3 The fitting procedure

In principle the decompositions can be performed by fitting all 31 variables simultaneously, but in practice this is not reasonable or even possible. Instead we proceed in steps where the orientation parameters are first fixed to the values obtained by fitting ellipses to the isophotes, as described in Section 3.1. Also, in order to have control of the physical meaning of the different components, *a priori* identification of the structural components is made while making the initial guesses for the fitted functions. If bars and ovals appear in the same galaxy, an attempt was made to avoid possible degeneracy between these components by using different types of radial profiles for bars and ovals. In some galaxies bars might have a thin rectangular component together with a thicker and shorter component, in which case it is possible to use two different functions for the bar. However, in this study it is not critical whether the thick component is part of the bar, or an oval inside the bar.

Our images are generally deep enough for reliable estimation of the scalelengths of the disk, but due to the 2D nature of the method the surface brightness profiles are often rather noisy. In principle a lower noise level could be achieved by rebinning the images, but in that case the advantage of the high image resolution is lost. Partly for this reason and also for saving time, the decompositions were performed in steps in the following manner:

(1) Generally the scalelength of the disk,  $h_r$ , was measured by doing bulge/disk decomposition for the image rebinned by a factor of 4, but if a prominent bar appeared in the galaxy, the bar was also fitted. *Seeing* was taken into account and a weighting function was selected to fit well particularly the exponential disk. Generally the pixels were weighted inversely proportional to Poisson noise (to  $1/|F_i|$ ), but in some cases  $w_i$  proportional to  $r_i$  was more useful. In most cases the images were deep enough for reliable estimation of  $h_r$ , but for the galaxies NGC 1415, NGC 2911, and NGC 4340, the obtained  $h_r$  is most probably underestimated.

(2) As a next step  $h_r$  was fixed and multicomponent decomposition was performed. In order to have a good fit in a reasonably short time the shape parameter describing deviations from elliptical isophotes was not used. Again, a Gaussian function was used in the decomposition to correct for *seeing*, and this time a weighting function was always taken to be inversely proportional to Poisson noise.

(3) Finally a decomposition including also a non-zero shape parameter  $c$  of the bulge and allowing for apparent bulge ellipticity was performed, using the previous solution for the initial parameters. The model functions were then subtracted from the original image and the residual image was inspected. If the residuals were too large the procedure was repeated a couple of times until a satisfactory solution was found. Taking into account the large number of free parameters in the fit it

was sometimes useful to repeat the decomposition several times fixing some of the parameters at each step.

#### 4.4 The decompositions for individual galaxies

The structural decompositions derived for the  $K_s$ -band images are shown for all galaxies in our sample in Fig. 4. We display the original and model images (upper and lower left panels, respectively), and the surface brightness profiles together with the model functions (right panel). Also, the residual images obtained by subtracting the model functions from the original images are shown in Fig. 5 (left panel). The most important parameters of the best fitting solutions are shown in Table 7. In the table the columns “Ferr 1”, “Ferr 2” and “Ferr 3” show the parameters of the Ferrers function, corresponding either to bars or ovals, depending on the physical components appearing in each galaxy. Bulge-to-disk light ratios in the table are given so that only the exponential component is included in the disk. However, it would be more realistic to use  $B/D_{tot}$ , where bars and ovals/lenses are also included to the disk (which can be calculated from the parameters given in the table). For NGC 3414 no decompositions were made, because it was not clear whether this is a face-on or edge-on galaxy. In general we take a conservative approach in a sense that if the evidence for a structural component is very weak, it is not included in the fit. This is a reasonable approach, because features with low surface brightnesses are not expected to have any effect on the  $B/T$ -ratio. In the following the decompositions for some individual galaxies are discussed.

**NGC 718:** Bulge/disk/bar decomposition was made, which gives a reasonable solution even if the central elliptical structure is not taken into account. In principle this solution gives an upper limit to the  $B/T$  light ratio, although most probably the central elliptical has only a minor effect on the relative mass of the bulge. In order to test the influence of the bar to the  $B/T$ -ratio, both a Ferrers’s and a Sérsic’s function were applied to the bar. The largest relative bulge mass was obtained using a flat Ferrers function ( $n_{bar} = 1$ ), which gave  $B/T = 0.23$ , whereas Ferrers’s function with  $n_{bar} = 4$  gave a similar relative bulge mass as obtained using a Sérsic’s function for the bar ( $B/T = 0.20$  and  $B/T = 0.18$ , respectively). In any case the type of function used to fit the bar appeared to have only a minor effect on the obtained  $B/T$  light ratio. The surface brightness profile of this galaxy looks interesting, because it shows an exponential-like behavior only in the outer part of the galaxy, whereas the surface brightness declines at the radius where the bar ends (at  $r = 25$  arcsec). The non-exponential disk is visible also in the residual image as negative pixels. The residual image also shows the flux of the spiral arms above the disk.

**NGC 936:** A decomposition was made which included a bulge, disk, bar and an oval. The fit to the surface brightness profile is quite good, but the residual image still shows some substructure with positive and negative pixels in the bar region. The substructure at the end of the bar is due to the flux condensation at the two ends of the bar. The positive residuals at

the outer edge of the disk indicate that the exponential disk fit is failing at large radii.

**NGC 1400:** The surface brightness profile of this galaxy is relatively simple, but no unambiguous solution was found because the fit did not converge. After several iterations the solution was changed only very slowly, until the disk was rapidly lost. However, the solution obtained by this manner was unsatisfactory, leaving a very large residual in the outer parts of the galaxy. The decomposition is very similar to the test case shown in Fig 3b, where the disk component was also rapidly lost after several iterations. The best solution was found by stopping the iteration slightly before the disk was lost, in which case the residuals are considerably smaller. For this galaxy, the solution was improved in the central regions when the shape parameter for the bulge was also used, indicating that the bulge is slightly flattened. As mentioned in Section 3.2, this might be the reason for the large  $A_2/A_0$ -ratio in the central part of this galaxy.

**NGC 1415:** All the previously identified structural components are visible in the surface brightness profile of this galaxy: the bar, the inner disk, the bulge and the outer disk, but the image does not have sufficient depth for reliable fitting of the outer disk. As a compromise the bar and the exponential disk were fitted by a single function, with the consequence that this decomposition can be used only as an approximation for the  $B/T$ -ratio, but not for estimating the scalelength of the disk (the disk parameters are not shown in Table 7).

**NGC 1440:** In addition to having a bar this galaxy has also a large lens, which in this particular galaxy somewhat affects the final decomposition. We found that including the lens to the decomposition considerably improves the final model and changes the relative mass of the bulge from  $B/T = 0.19$  to  $B/T = 0.14$ . The residual image shows that both the bar and the lens are fairly well subtracted.

**NGC 1452:** Reasonable solutions for the surface brightness profile of this galaxy can be found both by applying a bulge/disk/bar or a bulge/disk/bar/oval decomposition. However, the model image is considerably improved if the oval is also included. Also, the exponent of  $n_{bar} = 1$  for the bar model gave the best fitting solution for the bar. The best fit was obtained by finding first a model for the thin rectangular bar, and then the parameters for the bulge and the oval were left free for fitting. This is one of the galaxies that seems to have a non-exponential disk under the bar region: it appears as a decline in the surface brightness profile, and also, as positive residuals in the image where the model is subtracted from the original image.

**NGC 2273:** This galaxy has an inner disk with such a high surface brightness that it can be identified in the surface brightness profile of the non-rebinned image (not well visible in the rebinned image in Fig. 4). However, due to the degeneracy between the functions describing the bulge and the inner disk we did not include it in the final decomposition. For this reason,

the obtained  $B/T$ -ratio can be taken as an upper limit. After subtracting the galaxy model from the observed image some residuals are left, demonstrating the presence of the spiral arms and an inner ring surrounding the bar.

**NGC 2460:** Decompositions for this galaxy have been made previously by Carollo et al. (1997), by Baggett, Baggett & Anderson (1998, hereafter BBA98) and by Peng et al. (2002), which offer interesting points of comparison with our decomposition. BBA98 used a 1D-method with a Sérsic's function for the bulge, and applied their method to profiles from photographic plates that had a large enough field of view for reliable estimation of the radial scalelength of the disk. They found that the exponential disk is either very weak or absent. On the other hand, Carollo et al. used optical HST-images and an  $R^{1/4}$  law function for the bulge: they comment that this galaxy most probably has a small bulge. The most sophisticated analysis for this galaxy was made by Peng et al., who applied a multicomponent 2D decomposition method to a high resolution HST-image. Including a bar, bulge and a disk in the solution, they obtained  $B/T=0.41$ , which is very similar to  $B/T = 0.38$  found in this study. This corresponds to a typical ratio for an Sa-type spiral (Simien & de Vaucouleurs 1986). We also fitted the bar, but it appeared to be unimportant for the obtained  $B/T$ -ratio.

**NGC 2681:** This galaxy has, in addition to a bulge and a disk, also 3 bars and a lens, which in principle all could be taken into account in the decomposition. We included only the two larger bars and the lens in the decomposition. The secondary bar near to the nucleus (visible in the non-rebinned image) has a surface brightness that is too close to the surface brightness of the bulge to be taken into account in the decomposition, so that the functions for the bulge and the secondary bar became degenerate.

**NGC 2859:** The best model was found by fitting, besides the bulge and the disk, also 2 bars and a lens. Owing to the complex structure of this galaxy the decomposition was performed in steps so that the radial scalelength of the disk was found first, then the parameters of the primary bar and the lens, and finally the parameters of the bulge and the secondary bar were left free for fitting.

**NGC 3626:** This galaxy was found to have a bar and an elliptical inner structure which might be a secondary bar or an inner disk. Reasonable decompositions can be made either by fitting both components or only the bar component, because the inner elliptical structure does not affect the obtained  $B/T$ -ratio. After subtracting the model from the original image the residuals are small, manifesting mainly the spiral structure of this galaxy.

**NGC 3941:** For this galaxy the parameters for the disk and the bar were found first, then they were fixed and the parameters for the bulge and the lens were found simultaneously. A test was also made of how much omission of the lens might affect the relative mass of the bulge: we found that the decomposition including the oval gives  $B/T = 0.17$ , while the

decomposition without a lens gives  $B/T = 0.22$ . In such a decomposition model the residuals are extremely small.

**NGC 4245:** This galaxy has two bars and a lens. The best solution was found in steps by fitting first the bulge, the disk and the bar. However, it was more difficult to fit the lens, which easily disappeared. Finally a solution for the lens was found by fixing its flux shortly before the component disappeared. The lens in this galaxy has a low surface brightness and does not affect the obtained  $B/T$ -ratio. The model-subtracted image shows positive residuals at the ends of the bar, hinting at the presence of ansae.

**NGC 4340:** This is again an example of a galaxy with a complicated structure having 2 bars and a lens, which were all fitted in the final decomposition. As usual, the solution was found in steps starting from the parameters of the disk and the primary bar, and then finding the parameters for the bulge and the secondary bar. Again, the ansae-type morphology of the bar is visible in the residual image.

**NGC 4643:** For this galaxy the best decomposition included, besides the bulge and the disk, also a bar and an oval. The bar model was improved using  $n_{bar} = 1$ . Also, automatic fitting created a slightly too long bar, so that the bar was forced to have a length that gave the smallest residuals. The automatic procedure easily makes a too long bar if there is an inner ring surrounding the bar.

It is difficult to compare our results with the previous studies mainly because in most cases different decomposition methods have been used. To our knowledge the only previous studies where multicomponent 2D decompositions have been used are the studies by Prieto et al. (2001) and Peng et al. (2002). With Prieto et al. we have no galaxies in common, whereas with Peng et al. there is one galaxy, NGC 2460, in common. As discussed above, for this galaxy a very similar  $B/T$ -ratio was found in both studies ( $B/T = 0.38$  and  $0.41$ ). A 2D decomposition method has been recently applied for S0s also by de Souza, Gadotti & dos Anjos (2004, hereafter SGA04) using a Sérsic's function for the bulge, but without including a bar in the fitted model. We have no galaxies in common with SGA04, but the method is similar as used by GS03 for NGC 4608. For this galaxy GS03 found a massive bulge but no clear sign of the disk component, whereas we found only a small bulge and a prominent disk with  $B/T = 0.15$  (see a detailed discussion in Section 5.2).

Another way of evaluating our decompositions is to compare the scalelengths of the disks with those obtained in other studies. We compare  $h_r$  estimated by us in the  $K_s$ -band with those obtained by BBA98 in the  $V$ -band (see Table 8 and Fig. 6). BBA98 have measurements for 16 galaxies common with our sample, of which 13 show reasonable agreement with our measurements. This is the case in spite of the fact that BBA98 used a 1D decomposition method, fitted a de Vaucouleurs's  $R^{1/4}$  function for the bulge, and used a truncated exponential for the disk. However, for NGC 936 we found a larger  $h_r$  than

BBA98 (36.8 v.s. 23.8), and for NGC 2911, NGC 2859 and NGC 4340 completely different  $h_r$  values were obtained (41.6 vs. 19.2; 78.2 vs. 18.8; 41.1 vs. 10.9, respectively). These differences seem to be more related to the depth of the images than to the difference in the decomposition method used: most probably for NGC 2859 BBA98 are looking at only the disk in the bar region, whereas our image shows also the outer disk. For NGC 4340 the reason for the different results between the two studies is not clear: a comparison with the Digitized Sky Survey image shows that for this galaxy our image is not very deep. In any case the very small  $h_r$  obtained by BBA98 must be an underestimate. Our measurements are uncertain for the galaxies that have extremely faint outer disks or prominent outer rings dominating the disk, which is the case for NGC 2781 and NGC 2859.

## 5 DISCUSSION OF THE DECOMPOSITIONS

Two main topics will be discussed in the following: (1) we compare our results for the  $B/T$ -ratios and the parameters of the bulge with those presented earlier in the literature and (2) discuss the possibility raised by GS03, that some barred S0s might lack the disk component. Particularly the galaxy NGC 4608 will be analyzed.

### 5.1 B/T-ratios and the bulge shapes

Structural decompositions for S0s have repeatedly pointed to a mean  $B/T$ -ratio of nearly 0.6 in the  $B$ -band, as reported also in the recent review by Fritze & Alvensleben (2004). This is a considerably larger value than  $\langle B/T \rangle = 0.41$  obtained by Simien & de Vaucouleurs (1986) for Sa-galaxies, which has been argued to indicate that S0s have relative bulge masses intermediate between ellipticals and early-type spirals. The  $B/T$ -ratio for S0s seems to depend very little on the type of function used for fitting the bulge: for example the de Vaucouleurs's  $R^{1/4}$  law has been used in the early studies by Burstein (1979), Simien & de Vaucouleurs (1986) and by Kent (1985), whereas the more general Sérsic's function has been recently used by SGA04, all giving similar  $B/T$ -ratios for S0s. The studies by Burstein and Simien & de Vaucouleurs were performed using  $B$ -band images, whereas Kent and SGA04 used  $R$ -band images. The results in the  $R$ -band can be converted to correspond to the  $B$ -band measurements by applying correction terms based on the theoretical models by Schulz et al. (2003, hereafter SFAF03). The corrections are based on the assumption that the star formation time scales are different for bulges and disks, and then spectral evolution in the wavelength range from UV to  $I$ -band is modeled in both components during the age of the galaxy. Different ages for the bulges and the disks are assumed, but the corrections for S0s are not much different if they have similar or different ages. In the  $R$ -band Kent found  $\langle B/T \rangle = 0.69$ , while SGA04 found  $\langle B/T \rangle = 0.64$ . After applying the wavelength dependent correction these values are converted to correspond to the  $B$ -band values  $\langle B/T \rangle = 0.59$  and

0.54, respectively, which are very similar to  $\langle B/T \rangle = 0.57$ , obtained by Simien & de Vaucouleurs in  $B$ -band. There is only one study, by APB95, where a lower  $\langle B/T \rangle = 0.32$  has been reported in the  $K$ -band for a small number of S0s. Also, for S0s in clusters a somewhat lower  $\langle B/T \rangle = 0.45$  has been recently reported by Christlein & Zabludoff (2004, hereafter CZ04) in  $R$ -band. In the studies where a Sérsic's function is used for the bulge, the shape parameter  $\beta$  of the bulge is found to be almost identical with that corresponding to the  $R^{1/4}$  law, which also explains why the  $B/T$ -ratios obtained in different studies can be so similar.

In this study we found  $\langle B/T \rangle = 0.24 \pm 0.11$  for S0s (14 galaxies) and  $\langle B/T \rangle = 0.28 \pm 0.14$  for Sa - S0/a galaxies (9 galaxies). The models by SFAF03 do not extend to the near-IR, but the  $B/T$ -ratios at  $K_s$ -band are expected to be more similar to those obtained in the  $R$ -band than those obtained in the  $B$ -band. The values found in this study are considerably smaller than reported in any of the previous studies, and are likely due to the fact that we have used a *multicomponent* decomposition method to estimate the  $B/T$ -ratios. The bulges in S0s were also found to be much more exponential-like than generally assumed: we found  $\langle n \rangle = 2.1 \pm 0.7$  (or  $\beta = 0.48$ ), compared to  $\langle n \rangle = 4.1$  (or  $\beta = 0.24$ ), given by SGA04 and APB95. The largest  $n$ -value in our sample is 3.4 indicating that none of the galaxies has a de Vaucouleurs's type surface brightness profile. This is in agreement with Balcells et al. (2003), who came to the same conclusion using HST-images for their analysis. The mean  $B/T$ -ratios for early-type disk galaxies in different studies are collected in Table 8, where the numbers in parentheses indicate the number of galaxies used in the statistics.

A question then arises why does our study provide such a different results compared to the previous studies? Our measurements for the  $B/T$ -ratios and  $n$ -values are compared with those obtained by APB95 and SGA04 in Fig. 7. It is particularly interesting to compare with the measurements by APB95, because the Kent's method for estimating the  $B/T$ -ratios is independent of any assumptions for the model functions. It was applied only for non-barred galaxies, for which this method should work well. It appears that for a given galaxy luminosity the  $B/T$ -ratios found by APB95 are very similar to those obtained in this study, whereas our  $n$ -values are systematically smaller. APB95 had originally a magnitude limited sample of 30 S0-Sbc galaxies (of which 7 were S0s), of which a subsample of 19 galaxies (including all morphological types) was selected for HST imaging (Balcells et al. 2003). For these galaxies Balcells et al. then combined the ground-based images with the resolution of  $0.29 \text{ arcsec pixel}^{-1}$  with the HST images. They applied a decomposition method using a Sérsic's function for the bulge and another function for a possible nucleus and found  $\langle n \rangle = 1.7$ , which is considerably smaller than  $\langle n \rangle = 3.0$  using their ground-based images alone. However, a comparison to SGA04 in Fig. 7 shows that both the  $B/T$ -ratios and the  $n$ -values found in this study are systematically smaller with practically no overlap between the two studies. This is not

a luminosity effect: the parameters of the bulge are not strongly correlated with galaxy luminosity, and we also have a large overlap in galaxy luminosity. For a given luminosity the  $n$ -values obtained by SGA04 are also larger than those by APB95.

The reason for the small  $B/T$ -ratios and  $n$ -values found in this study are most likely related to the decomposition method, which takes into account not only the bulge and the disk, but also bars and ovals, which might otherwise be erroneously mixed with the flux of the bulge. Indeed, if the fluxes of the bars/ovals were added to the flux of the bulge, we would obtain  $B/T=0.41$ , which is expected to mimic the previous bulge/disk decompositions for early-type galaxies. Other minor factors that might affect the  $B/T$ -ratio are the image resolution and the weighting function applied for noisy images. For noisy images mixing with the bulge might occur particularly if a weighting function giving more weight to the inner parts of the galaxy is used. It was pointed out by the referee that probably the largest uncertainty in our multicomponent decomposition method is the fact that the bar morphologies are not well known, which might partly explain the low  $B/T$ -ratios found in this study. Indeed, boxy/peanut shaped bars are found in galaxies when viewed edge-on (Lütticke, Dettmar & Pohlen 2000), and some bars particularly in early-type galaxies have ansae-type morphologies, where the surface brightness increases towards the outer edges of the bar. Theoretical models based on N-body simulations (Athanasoula 2005 and references therein) also produce this kind of bar: in these models the inner parts of the bars originally have nearly the same vertical thicknesses as the outer parts of the bars, but the vertical thickness in the inner bar regions increases in time.

In our sample there are many galaxies having bars with ansae-type morphologies. In the decompositions they appear as faint positive residuals at the two ends of the bar (Fig. 5). These structures are faint and their flux is also later added to the flux of the disk, so that they are not expected to affect the obtained  $B/T$ -ratio. As the galaxies in our sample are not edge-on systems, it might be difficult to distinguish possible thick inner portions of the bars from other thick components like ovals/lenses. However, this is not critical for our purposes (for  $B/T$ -ratio), because in both cases we have used two different functions in the decompositions. However, if we for some reason have missed the thick part of the bar, that would mean that we have underestimated the bar flux and therefore also overestimated the  $B/T$ -ratio.

There still remains the uncertainty that we have interpreted a bar seen end-on as a small bulge, which in the simulation models by Athanasoula (2005) has the properties of a classical bulge. However, as bars are randomly oriented in space such cases should be rare. Another possible uncertainty is the surface brightness profile of the primary bar in the presence of the secondary bar: does it have a truncated inner structure, induced by secular evolutionary processes in the galaxy? The present simulation models do not give an answer to this question, but even if the primary bars were assumed to have a truncated profile, it is not expected to have any important implications to the  $B/T$  flux ratio. For example, NGC 2859 has both a



primary bar and a secondary bar. If the secondary bar is included to the decomposition  $B/T = 0.27$ , and if it is not included,  $B/T = 0.30$ . As the surface brightness of the primary bar in this particular galaxy is 2 magnitudes fainter than that of the secondary bar, excluding its flux in the region of the secondary bar cannot have any effect to the  $B/T$ -ratio. In our sample we have 4 galaxies with detectable secondary bars. For two of them (NGC 718, 2681) it was not taken into account in the decomposition, and two of them (NGC 2858, 4340) the effect of the secondary bar to the  $B/T$  flux ratio was minimal.

## 5.2 NGC 4608: a barred S0 without a disk?

NGC 4608 is one of the two galaxies which have been discussed as examples of S0s having prominent bars, but no clear sign of an underlying disk (GS03)<sup>1</sup>. Structural decompositions for this galaxy has been made by GS03 both in the optical and in the near-IR, of which the decomposition in the  $V$ -band was shown by Gadotti & Souza (2002, their Fig. 1). They used a 2D decomposition method with an exponential function for the disk and a Sérsic's function for the bulge. The resolution in their  $V$ -band image is  $0.3 \text{ arcsec pixel}^{-1}$  and the fitting region  $r_{max} = 135 \text{ arcsec}$ , which can be estimated from their figure. As we also have a  $V$ -band image for this galaxy, having a slightly better resolution of  $0.19 \text{ arcsec pixel}^{-1}$ , we try to verify their result first.

Bulge/disk decomposition was performed for the rebinned  $V$ -band image using an exponential function for the disk and a Sérsic's function for the bulge (Fig. 8a). By limiting the maximum fitting region to  $r_{max} = 135 \text{ arcsec}$ , we found a solution having a relatively small bulge with  $B/T = 0.38$ . Possible effects of the weighting function for the solution were investigated. We used the different weighting functions described in Section 4.1 and found that in all cases where a convergence resulted, the  $B/T$ -ratio depended only slightly on the weighting method: the  $B/T$ -ratio varied between 0.38-0.42 for different weighting functions. In the residual image (bottom panel of Fig. 8a) the non-subtracted bar is visible as a black feature, and the white region inside the radius of the bar indicates that too much disk is subtracted in that region (interpreted as a lack of a disk by GS03). The only way of fitting the surface brightness profile mostly by one single function (as in GS03) was to give strong weight for the inner galaxy region using weighting proportional to  $1/r$ . However, in that case the solution did not converge and a jump to a single function solution occurred rapidly in a similar manner as in our test shown in Fig. 3b. As in the test case, also in this case the residuals after subtracting the bulge were larger than in the solutions where the fit converged. Gadotti & Souza do not specify the weighting function they used for NGC 4608, but the solution is not expected to depend strongly on the weighting function used.

<sup>1</sup> This interpretation has been changed by SGA04: in the discussion part of their paper the disk of NGC 4608 is considered to be absent only within the radius of the bar.

Finally the decomposition was improved by including, besides the bulge and the disk, also the bar and the lens for which Ferrers functions were used (Fig. 8b). In that case we obtained  $B/T = 0.19-0.22$  for the rebinned image, depending on the choice of the weighting function. As a further test for the reliability of the solution, the models for the bar and the lens were subtracted from the original image, and then a bulge/disk decomposition was made for this residual image (Fig. 8c): in that case we found  $B/T = 0.22$ , which is the same as the value obtained by fitting all three components simultaneously. It seems that omitting the bar in the decomposition causes the  $B/T$ -ratio to be overestimated by about 40 %. The solution does not depend on the wavelength used: in the  $K_s$ -band we found  $B/T = 0.19$  for the rebinned image, and  $B/T = 0.15$  using the original high resolution image. In these decompositions  $h_R$  was fixed to the previously found value, for the bar we used  $n_{bar} = 2$  and for the oval  $n_{oval} = 3$ . In this case the shape parameter  $c_{bulge}$  was fixed to give elliptical isophotes, but all the other parameters like the ellipticity of the bulge, were left free for fitting. Our solution with a small bulge for NGC 4608 also corresponds to the visual impression in the original image: the galaxy has a small spherical component in the central part of the galaxy and a lens with a different ellipticity at a radius which is smaller than the radius of the bar. Even if the lens were interpreted as part of the bulge, the bright part of the spheroidal component would still be small compared to the size of the bar.

We have displayed the surface brightness profile in such a manner that in principle all pixels of the 2D image can be shown, which makes it possible to better evaluate the presence of the disk. The profile (Fig. 8 uppermost row) shows a prominent underlying disk which is exponential in the outer parts of the galaxy, but under the bar region at  $r < 45$  arcsec (in the bar minor axis direction) the surface brightness of the disk rapidly declines: e.g. the lower part of the profile declines, although due to the bar the total surface brightness at the same radius increases. The non-exponential nature of the disk under the bar region is clearly visible also in the residual image where the model functions are subtracted from the original image (in all three decompositions): inside the radius of the bar too much flux is subtracted, being manifested as negative residuals in the image. The residual image also shows faint ring-like structures outside the bar. In the outermost part of the image ( $r > 100$  arcsec) subtraction of the exponential disk is not very good anymore, mainly because the surface brightness profile starts to show signs of outer truncation. If we assume that the inner disk is truncated inside the radius of  $r < 20$  arcsec, which is the crossing point of the bulge and disk models, the  $B/T = 0.27$  is obtained. This is an upper limit for the  $B/T$ -ratio and, in spite of the non-exponential nature of the inner disk, most probably an overestimation of the  $B/T$ -ratio. It is not yet clear whether this kind of non-exponential inner disks are typical for S0s.

Our conclusion is that, contrary to the previous claim by GS03, NGC 4608 has only a small bulge and a prominent

disk. The disk is exponential outside the bar and non-exponential in the bar region, where it is about 0.5 mag fainter than expected if the exponential outer disk is extrapolated to the bar region. In our decomposition the bulge contribution is already negligible at the distance of the end of the bar ( $r = 35''$ ), where only the disk and the bar are contributing to the observed surface brightness. The non-exponential nature of the disk in this galaxy is interesting and might be a manifestation of secular evolutionary processes as predicted by the theoretical models by Athanassoula (2003) and Athanassoula & Misiroidis (2003). GS03, based on finding no disk component in this galaxy, reach the same conclusion. A similar non-exponential disk under the bar region was found also in NGC 718, and probably also in NGC 1452.

## 6 SUMMARY AND CONCLUSIONS

A 2D multicomponent decomposition method has been applied to a sample of 24 early-type disk galaxies using deep high resolution  $K_s$ -band images obtained at the NOT. The sample, consisting of 14 S0s and 9 early-type spirals, is part of our magnitude limited NIRS0S sample of 170 early-type disk galaxies. The decompositions were performed using an exponential disk and a Sérsic's function for the bulge, while bars and ovals were fitted either using a Sérsic's or Ferrers's functions. The effect of *seeing* was taken into account by convolving the model images with a Gaussian PSF, and the method also allowed deviations from elliptical isophotes. Finally the decomposition method could be successfully applied only for 22 galaxies: NGC 3414 appeared to be a misclassified edge-on galaxy, and for NGC 1415 the decomposition was too uncertain for reporting the B/T-ratio in a reliable manner. In order to avoid non-physical solutions for some S0s with complex morphological structures, *a priori* identification of the structural components was made by inspecting the radial profiles of the orientation parameters, derived by fitting ellipses to  $B$ -band images, and by inspecting the radial profiles of the Fourier amplitudes and phases. Also, in order to distinguish secondary bars from inner disks, unsharp masks were created, which work as a filter suppressing the low frequency variations in the images. Inner spiral arms, not reported previously in the literature, were found for the galaxies NGC 1415 and NGC 3941.

The decomposition method was first tested by creating synthetic images imitating real galaxies, for which the decomposition method was applied in a similar manner as for the science images. Particularly we tested how much omission of a prominent bar affects the obtained B/T-ratio, how important is the weighting function used, and what are the effects of *seeing* in the decomposition. We found that, by omitting a prominent bar in the decomposition, the relative mass of the bulge may be overestimated by as much as 30-40 %. The exact choice of the weighting function was not found to be important unless the images were extremely noisy or if simple two-component decompositions were applied for galaxies with prominent bars. The effects of *seeing* can be properly corrected in our method once the PSF in the image is well known. However, if

no *seeing* correction is made the  $\beta$  parameter of the bulge will be overestimated and the profile that originally had a de Vaucouleurs's type profile starts to approach an exponential profile.

Our most important result is that S0s have bulges that have much smaller relative masses than previously assumed. We found  $\langle B/T \rangle_K = 0.24 \pm 0.11$  ( $N = 14$ ), compared to  $\langle B/T \rangle_R = 0.6$  as reported in most previous studies. The most likely reason for the low B/T-ratio found in this study is our improved decomposition method, which takes into account, not only the bulges and disks, but also bars and ovals. Indeed, if the flux of the bars and ovals were included to the flux of the bulge, we obtain  $\langle B/T \rangle = 0.41$ , which would be close to the value found previously for early-type galaxies in clusters (CZ04). It also appeared that the bulges of S0s do not follow the  $R^{1/4}$  law profiles as generally assumed. Instead we found  $\langle n \rangle = 2.1 \pm 0.7$  (or  $\beta = 0.48$ ), compared to  $\langle n \rangle = 4.1$  (or  $\beta = 0.24$ ) found for example by SGA04 and APB95. We did not find examples of barred S0s lacking the disk component. Two such cases had been previously discussed by GS03, of which NGC 4608 was analyzed in this study. For this galaxy we found  $B/T = 0.38$ , if only the bulge and the disk were taken into account in the decomposition, and more realistically  $B/T = 0.15$  if the bar and the lens were also included in the fit. This galaxy was also found to have a non-exponential inner disk, which might be a manifestation of secular evolution as predicted by the models by Athanassoula (2003) and Athanassoula & Misiroidis (2003). Another similar case was NGC 718, and possibly also NGC 1452. Quite interestingly S0/a - Sa galaxies in our sample were found to have similar  $B/T$ -ratios ( $\langle B/T \rangle_K = 0.28 \pm 0.14$  ( $N = 9$ )) as the S0s. To our knowledge our study is the first attempt to apply 2D multicomponent decomposition method for a medium sized sample of early-type disk galaxies.

## ACKNOWLEDGMENTS

We thank the anonymous referee for a careful reading of the manuscript. EL and HS acknowledge the support of the Academy of Finland, and EL also from the Magnus Ehrnrooth Foundation. This research has also made use of the NASA/IPAC Extragalactic Database (NED) which is operated by the Jet Propulsion Laboratory, California Institute of Technology, under contract with the National Aeronautics and Space Administration. RB also acknowledges the support of NSF grant AST 0205143 to the University of Alabama.

## REFERENCES

- Andredakis Y. C., Peletier R. F., Balcells M., 1995, MNRAS, 275, 874 (APB95)
- Athanassoula E., Morin S., Wozniack H., Puy D., Pierce M. J., Lombard J., Bosma A., 1990, MNRAS, 245, 130
- Athanassoula E., 2002, ApJ, 569, 83

- Athanassoula E., 2003, MNRAS, 341, 1178
- Athanassoula E., 2005, astro-ph/0501196
- Athanassoula E., Misiioritis, 2003, MNRAS, 330, 35
- Baggett W. E., Baggett S. M., Anderson K. S. J., 1998, ApJ, 116, 1626 (BBA98)
- Balcells M., Graham A. W., Dominquez-Palmero L., Peletier R., 2003, ApJ, 582, L79
- Bekki K., 1995, MNRAS, 276, 9
- Bekki K., Warrick J., Yasuhiro S., 2002, ApJ, 577, 651
- Binney J., Tremaine S., 1987, Galactic Dynamics, Princeton University Press
- Burstein D., 1979, ApJ, 234, 435
- Buta R., Combes F., 1996, FCPH, 17, 95
- Buta R., Laurikainen E., Salo H., 2004, AJ, 127, 279
- Buta R., McCall, M. L., 1999, ApJ, 124, 33
- Byun Y. I., Freeman K. C., 1995, ApJ, 448, 563
- Caon N., Capaccioli M., D'Onofrio M., 1993, MNRAS, 265, 1013
- Carollo C. M., 1999, ApJ, 523, 566
- Carollo C. M., Stiavelli M., de Zeeuw P. T., Mack J., 1997, AJ, 114, 2366
- Christlein D., Zabludoff A. I., 2004, ApJ, 616, 192 (CZ04)
- D'Onofrio M., Capaccioli M., Caon N., 1994, MNRAS, 271, 523
- de Souza R. E., Gadotti A. S., dos Anjos S., 2004, ApJS, 153, 411 (SGA04)
- de Vaucouleurs G., de Vaucouleurs A., Corwin H. G., Buta R. J., Paturel G., Fouqué P., 1991, Third Reference Catalog of Bright Galaxies (New York: Springer) (RC3)
- de Jong R., 1996, A&A, 313, 45
- Eggen O. J., Lynden-Bell D., Sandage A. R., 1962, ApJ, 136, 748
- Elmegreen B., Elmegreen D., 1985, ApJ, 288, 438
- Erwin P., 2004, A&A, 415, 941
- Erwin P., Sparke L. S., 1999, ApJL, 521, 37
- Erwin P., Sparke L. S., 2003, ApJS, 146, 299 (ES03)
- Erwin P., Beckman J. E., Beltran J. C. V., 2004, astro-ph/0409103
- Erwin P., Beltran J. C. V., Graham A. W., Beckman J. E., 2003, ApJ, 597, 929
- Eskridge P. et al. 2002, ApJS, 143, 73
- Firmani C., Avila-Rees V., 2003, RMxAC, 17, 107
- Fritze U., Alvensleben V., 2004, astro-ph/0407358
- Gadotti D. A., de Souza R. E., 2002, Astr. Space Sci, 284, 527
- Gadotti D. A., de Souza R. E., 2003, ApJ, 583L, 75 (GS03)

- Garcia-Barreto J. A., Moreno E., 2000, ApJ, 529, 832
- Chitre A., Jog C. I., 2002, AA, 388, 407
- Jedrzejewski R. I., 1987, MNRAS, 226, 747
- Kormendy J., 1979, ApJ, 227, 714
- Kormendy J., Kennicutt R. C. Jr., 2004, Ann Rev. Astr. Ap., Vol. 42, 603 (KK04)
- Kent S. M., 1985, ApJS, 59, 115
- Laurikainen E., Salo H., 2002, MNRAS, 337, 1118
- Laurikainen E., Salo H., Buta R., Vasylyev S., 2004, MNRAS, 355, 1251 (LSBV04)
- Laurikainen E., Salo H., Buta R., 2004, ApJ, 607, 103
- Lütticke, R., Dettmar P.J., Pohlen M., 2000, AA 362, 435
- MacArthur A. A., Courteau S., Holtzman J., 2003, ApJ, 582, 689
- Malin D. F., Zealey W. J., 1979, Sky & Tel, 57, 354
- Möllenhoff C., Heidt J., 2001, A&A , 368, 16
- Peng C. Y., Ho L. C., Impey C. D., Rix H., 2002, AJ, 124, 266
- Prieto, M., Aquerri, J.A.L., Varela A.M., Munoz-Tunon C., 2001, AA, 367, 405
- Salo H., Rautiainen P., Buta R., Purcell G. B., Cobb M. L., Crocker D.A., Laurikainen E., 1999, AJ, 117, 792
- Samland M., Gerhard O. E., 2003, AA, 399, 961
- Sellwood J. A., 2000, Ap&SS, 272, 31
- Schulz J., Frize U., Alvensleben v., Fricke, K.J., 2003, A&A, 398, 89 (SFAF03)
- Sersic J. L., 1968, Atlas de Galaxias Australes. Observatorio Astronomico, Cordoba.
- Shaw M. A., Gilmore G., 1989, MNRAS, 237, 903
- Sil'chenko O. K., Afanasiev V. L., AJ, 127, 2641
- Simard L., et al., 2002, ApJS, 142, 1
- Simien F., de Vaucouleurs G., 1986, ApJ, 302, 564
- Toomre A., 1977, In "The Evolution of Galaxies and Stellar Populations, ed. B. M. Tinsley, R. B. Larson, p. 401
- Wadadekar Y., Robbason B., Kembhavi A., 1999, AJ, 117, 1219
- Whitmore B. C., Lucas R. A., McElroy D. B., Steinman-Cameron T. Y., Sackett P. D., Olling R.P., 1990, AJ, 100, 1489
- Wozniak H., Friedli D., Martinet P., Bratschi P., 1995, A&A, 111, 115

## 6.1 Figure captions

**Figure 1:** Polar angle maps of all  $K_s$ -band images of our sample. The x-axis is the angle from the line of nodes counted along the disk plane, and the y-axis is the distance from the galaxy center in arcseconds. In order to better illustrate the non-axisymmetric features, the axisymmetric  $m = 0$  components are subtracted from the original images. We also show the  $m = 2$  and  $m = 4$  Fourier amplitudes of density, normalized by the  $m = 0$  component, and their phases. The images we use were deprojected to face-on orientation as explained in Section 3.2.

**Figure 2:** *Test a* shows bulge/disk decomposition for a synthetic image having an exponential disk with  $h_r = 45$  and a Sérsic bulge with  $\beta = 0.6$  and  $h_b = 1$ . In order to imitate realistic galaxy images, Poisson noise and background noise were also added. *Tests b* and *c* show decompositions for a synthetic image in which bar component, described by a Ferrers function, was also added. In *test b* only the bulge and the disk were fitted, whereas in *test c* all three components were fitted simultaneously. In the surface brightness profile, each pixel in the image is shown as a function of its distance from the center measured in the sky plane (*black dots*). Also shown are the model components for the bulge and the disk (*light grey*), for the bar (*darker grey*), and for the total model (*dark grey*). For each decomposition, the synthetic image, model image, and residual (difference) image are also shown.

**Figure 3:** Decompositions were made for three synthetic images with a Sérsic's bulge and an exponential disk with  $h_R = 50$ . As in Fig. 2 Poisson noise and background noise were also added. The two synthetic images in tests *a* and *b* were taken to have nearly  $R^{1/4}$  like total surface brightness profiles, but different properties of the bulge, as indicated in the figure. The third synthetic image was used in tests *c* and *d*, having a small bulge and a large and noisy disk ( $h_R = 50$ ). Two decompositions were made for this image, which were otherwise similar but deviated in the choice of the weighting function: in *test d* pixels were weighted in proportion to  $1/F_i$ , whereas in *test c* they were weighted in proportion to  $r_i$ .

**Figure 4:** Multicomponent 2D decomposition applied to  $K_s$ -band images for all galaxies in our sample. In order to better illustrate the decompositions, the images were first rebinned by a factor of 4. Notice however, that in Table 6, where the final results are given, non-rebinned images were used. For each galaxy we show the observed image (*upper left panel*), the image constructed from the model functions, shown in the same orientation (*lower left panel*), and the surface brightness profile together with the fitted model functions (*right panel*). The colors in the profiles are the same as in Fig. 2, except that more components are shown. The zero point of the surface brightness is arbitrary, but one unit corresponds to one magnitude.

**Figure 5:** Residual images for all galaxies. In the *left panels* are shown the residual images from the decompositions, obtained by subtracting the model images from the observed images. In the *middle panel* are shown the unsharp masks, created by subtracting a heavily smoothed copy from the original image. The unsharp masks (positive parts) are shown in a logarithmic scale with contours over-plotted on the images for better illustrating the faint structural components in the galaxies. The x- and y-coordinates in both images are given in arcseconds. In the *right panel* are also shown the radial profiles of the position angles  $\phi$  and the minor-to-major axis ratios  $q$  for these galaxies, shown on a logarithmic radial scale. The residual images are obtained using the  $K_s$ -band images, whereas the radial profiles for the orientation parameters were derived mainly using the  $B$ -band images (see Table 2). Notice that for the unsharp mask images, only the central parts of the images are shown.

**Figure 6:** The scalelengths of the disks obtained in this study in the  $K_s$ -band are compared with those obtained by Baggett, Baggett & Anderson (1998) in the  $V$ -band (NGC 2859 is outside of the figure). The line is a unit slope.

**Figure 7:** The parameters of the bulge found in this study are compared with those obtained by Andredakis, Peletier & Ballcells (1995, APB) who used a modified Kent’s method applied in the  $K_s$ -band, and with those obtained by de Souza, Gadotti & dos Anjos (2004, SGA) in the  $R$ -band using a 2D method with an exponential function for the disk and a Sérsic’s function for the bulge. The *thick crosses* show our measurements for S0s and the *thin crosses* are our measurements for S0/a - Sa galaxies. The *triangles* indicate the measurements by APB, whereas the *squares* show the measurements by SGA. The *upper panel* shows the shape parameter of the bulge,  $n$ , as a function of the  $B/T$ -ratio, and in the two lower panels  $B/T$  and  $n$  are shown as a function of galaxy luminosity. The estimated uncertainty in the  $n$  parameter in our study is 20%, based on the evaluation of the effect of the weighting function in the decomposition applied for noisy test images. The  $B$ -band magnitudes used to calculate the absolute magnitudes are from RC3. Note that the dispersion is large in the two lower panels, where the dependence of these parameters of the galaxy magnitude was studied.

**Figure 8:** Structural decompositions for NGC 4608 in the  $V$ -band. The left column (*Fig. 8a*) shows the bulge/disk decomposition, whereas in the middle column (*Fig. 8b*) the bar component is also added to the fit. *Fig. 8c* shows a decomposition made for the residual image obtained after subtracting the fitted bar/oval models from the original image. For all decompositions, the original, model, and residual images are also shown.



**Table 1.** Observations.

Galaxy	RC3 type	filter	FWHM [arcsec]	nuclear act.	
NGC 718	SAB(s)a	$K_s$	1.06	HII/SB	
		$B$	1.29		
NGC 936	SB(rs)0 <sup>+</sup>	$K_s$	1.24		
		$B$	1.31		
NGC 1022	(R')SB(s)a	$K_s$	1.84		
		$B$	0.99		
NGC 1400	SA0 <sup>-</sup>	$K_s$	1.06		
		$B$	1.25		
NGC 1415	(R)SAB(s)0/a	$K_s$	1.15		
		$B$	1.20		
NGC 1440	(R')SB(rs)0 <sup>o</sup> :	$K_s$	0.99		
NGC 1452	(R')SB(r)0/a	$K_s$	1.04		
		$B$	1.41		
NGC 2196	(R')SA(s)a	$K_s$	1.40		
		$B$	1.16		
NGC 2273	SB(r)a:	$K_s$	1.31		
NGC 2460	SA(s)a	$K_s$	0.99		
NGC 2681	(R')SAB(rs)0/a	$K_s$	1.15		Sy
		$B$	1.10		
NGC 2781	SAB(r)0 <sup>+</sup>	$K_s$	0.90		
NGC 2855	(R)SA(rs)0/a	$K_s$	0.92		
		$B$	1.39		
NGC 2859	(R)SB(r)0 <sup>+</sup>	$K_s$	0.92	Sy	
		$B$	0.82		
NGC 2911	SA(s)0: pec	$K_s$	0.78	Sy/L	
NGC 2983	SB(rs)0 <sup>+</sup>	$K_s$	0.97		
NGC 3414	S0 pec	$K_s$	1.01		
		$B$	1.14		
NGC 3626	(R)SA(rs)0 <sup>+</sup>	$K_s$	0.83		
NGC 3941	SB(s)0 <sup>o</sup>	$K_s$	0.87	Sy2	
NGC 4245	SB(r)0/a:	$K_s$	0.99	HII	
		$B$	0.91		
NGC 4340	SB(r)0 <sup>+</sup>	$K_s$	1.04		
		$B$	1.88		
NGC 4596	SB(r)0 <sup>+</sup>	$K_s$	0.85	L	
		$B$	1.31		
NGC 4608	SB(r)0 <sup>o</sup>	$K_s$	1.10		
		$B$	0.89		
NGC 4643	SB(rs)0/a	$K_s$	0.97	L	

**Table 2.** The orientation parameters

Galaxy	$\phi$ (measured) [ $^\circ$ ]	$q$ (measured)	range [arcsec]	filter	$\phi$ (RC3) [ $^\circ$ ]	$q$ (RC3)	$\phi$ (ES03) [ $^\circ$ ]	$q$ (ES03)
(1)	(2)	(3)	(4)	(5)	(6)	(7)	(8)	(9)
NGC 718	$7.4 \pm 2.5$	$0.852 \pm 0.014$	80-95	<i>B</i>	45	0.871	5	0.87
NGC 936	$122.7 \pm 1.6$	$0.739 \pm 0.009$	170,180	<i>B</i>		0.871	130	0.76
NGC 1022	$26.7 \pm 2.5$	$0.930 \pm 0.016$	88-115	<i>B</i>		0.832	174	0.92
NGC 1400	$37.1 \pm 5.3$	$0.915 \pm 0.013$	100-120	<i>B</i>	40	0.871		
NGC 1415	$151.7 \pm 0.5$	$0.390 \pm 0.005$	160-180	<i>B</i>	148	0.513		
NGC 1440	$22.2 \pm 2.5$	$0.777 \pm 0.026$	60-70	<i>K<sub>s</sub></i>		0.759		
NGC 1452	$113.4 \pm 0.8$	$0.698 \pm 0.010$	90-100	<i>B</i>	113	0.661		
NGC 2196	$67.8 \pm 1.5$	$0.697 \pm 0.012$	130-140	<i>B</i>	35	0.776		
NGC 2273	$59.3 \pm 1.2$	$0.599 \pm 0.016$	65-68	<i>K<sub>s</sub></i>		0.759	50	0.66
NGC 2460	$29.5 \pm 3.1$	$0.750 \pm 0.027$	45-55	<i>K<sub>s</sub></i>		0.759		
NGC 2681	$102.0 \pm 5.9$	$0.912 \pm 0.017$	120-145	<i>B</i>		0.912	140	0.95
NGC 2781	$72.0 \pm 2.0$	$0.515 \pm 0.012$	45-55	<i>K<sub>s</sub></i>		0.501		
NGC 2855	$107.2 \pm 2.7$	$0.838 \pm 0.011$	140-150	<i>B</i>	130	0.891		
NGC 2859	$86.3 \pm 1.3$	$0.760 \pm 0.012$	160-175	<i>B</i>	85	0.891	90	0.90
NGC 2911	$133.4 \pm 3.6$	$0.763 \pm 0.021$	30-35	<i>K<sub>s</sub></i>		0.776		
NGC 2983	$91.1 \pm 0.9$	$0.578 \pm 0.016$	65-70	<i>K<sub>s</sub></i>		0.589		
NGC 3414	$22.7 \pm 2.7$	$0.856 \pm 0.014$	110-120	<i>B</i>		0.724		
NGC 3626	$158.9 \pm 0.8$	$0.663 \pm 0.011$	70-73	<i>K<sub>s</sub></i>		0.724		
NGC 3941	$6.9 \pm 0.8$	$0.651 \pm 0.013$	70-80	<i>K<sub>s</sub></i>		0.661	10	0.65
NGC 4245	$174.1 \pm 2.2$	$0.823 \pm 0.011$	110-127	<i>B</i>		0.759	0	0.75
NGC 4340	$98.6 \pm 1.3$	$0.556 \pm 0.012$	150-165	<i>B</i>		0.794		
NGC 4596	$116.0 \pm 0.5$	$0.716 \pm 0.007$	160-175	<i>B</i>		0.741		
NGC 4608	$101.0 \pm 3.5$	$0.856 \pm 0.015$	130-150	<i>B</i>		0.832		
NGC 4643	$49.8 \pm 5.6$	$0.836 \pm 0.023$	100-105	<i>K<sub>s</sub></i>		0.741	55	0.80

The columns are: (1) the galaxy name, (2, 3) the measured position angle  $\phi$  and minor-to-major axis ratio  $q$ , (4, 5) the range and filter used for the measurements, (6, 7)  $\phi$  and  $q$  as given in RC3, (8, 9)  $\phi$  and  $q$  as given by ES03.

**Table 3.** The identified structural components.

Galaxy	primary bar	other components
NGC 718	<i>bar</i> (20 arcsec)	<i>bar</i> <sub>2</sub> or nuclear spirals
NGC 936	<i>bar</i> (55 arcsec)	nuclear ring (8-9 arcsec), lens
NGC 1022	<i>bar</i> (25-30 arcsec)	oval, inner pseudoring
NGC 1400		
NGC 1415	<i>bar</i> (70 arcsec)	inner spirals (9 arcsec)
NGC 1440	<i>bar</i> (30 arcsec)	lens
NGC 1452	<i>bar</i> (46 arcsec)	oval, ring
NGC 2196		inner elliptical (16 arcsec)
NGC 2273	<i>bar</i> (20 arcsec)	inner spirals (5 arcsec)
NGC 2460		<i>bar</i> <sub>2</sub> (8 arcsec)
NGC 2681	<i>bar</i> <sub>1</sub> (20 arcsec)	<i>bar</i> <sub>2</sub> (5 arcsec), <i>bar</i> <sub>3</sub> (60 arcsec), lens
NGC 2781	<i>bar</i> (45 arcsec)	inner spiral arms (10 arcsec)
NGC 2855		
NGC 2859	<i>bar</i> <sub>1</sub> (57 arcsec)	<i>bar</i> <sub>2</sub> (8 arcsec), two lenses, outer ring
NGC 2911		
NGC 2983	<i>bar</i> (36 arcsec)	inner elliptical (5 arcsec), lens
NGC 3414		lens
NGC 3626	<i>bar</i> (40 arcsec)	inner bar or a disk (5 arcsec), two lenses
NGC 3941	<i>bar</i> (30 arcsec)	inner spirals (4 arcsec), lens
NGC 4245	<i>bar</i> <sub>1</sub> (46 arcsec)	nuclear ring, inner ring, lens
NGC 4340	<i>bar</i> <sub>1</sub> (75 arcsec)	<i>bar</i> <sub>2</sub> (10 arcsec), lens
NGC 4596	<i>bar</i> (74 arcsec)	inner elliptical (7 arcsec), lens
NGC 4608	<i>bar</i> (55 arcsec)	inner ring, lens
NGC 4643	<i>bar</i> (60 arcsec)	possible nuclear ring (10 arcsec), lens

**Table 4a.** The effect of the weighting method when  $S/N = 3.0$ .

weight	$h_R$	rel. error	$B/D$	$\beta$	$r_{eff}$
$1/r^2$	27.96	-6.80 %	0.206	0.533	2.950
$1/(F_{model}r^2)$	29.83	-0.56 %	0.203	0.508	2.963
$1/r$	29.55	-1.49 %	0.202	0.515	3.005
<i>const</i>	29.91	-0.30 %	0.204	0.505	3.021
$1/(F_{model}r)$	29.98	-0.07 %	0.205	0.502	2.999
$r$	30.00	-0.01 %	0.205	0.499	3.002
$1/F_{model}$	30.02	+0.07 %	0.205	0.495	3.004
$r/(F_{model})$	30.05	+0.15 %	0.207	0.478	2.990
$1/(Fr^2)$	29.35	-2.18 %	0.207	0.512	3.004
$1/(Fr)$	29.55	-1.50 %	0.208	0.503	2.990
$1/F$	29.67	-1.10 %	0.210	0.493	3.009
$r/F$	29.87	-0.45 %	0.215	0.448	3.027

**Table 4b.** The effect of the weighting method:  $S/N=1.5$ 

weight	$h_R$	rel. error	$B/D$	$\beta$	$r_{eff}$
$1/r^2$	26.09	-13.03 %	0.209	0.564	2.921
$1/(F_{model}r^2)$	29.78	-0.73 %	0.203	0.511	3.062
$1/r$	29.03	-3.24 %	0.201	0.531	3.007
<i>const</i>	29.82	-0.60 %	0.203	0.510	3.045
$1/(F_{model}r)$	29.95	-0.16 %	0.204	0.503	3.000
$r$	30.00	-0.00 %	0.205	0.496	3.006
$1/F_{model}$	30.04	+0.12 %	0.206	0.492	3.006
$r/(F_{model})$	–				
$1/(Fr^2)$	27.91	-7.0 %	0.216	0.527	2.994
$1/(Fr)$	28.41	-5.3 %	0.220	0.506	2.916
$1/F$	28.80	-4.0 %	0.225	0.473	3.049
$r/F$	29.41	-2.0 %	0.244	0.379	3.237

**Table 5.** The effect of seeing in the estimated  $\beta$ . Subscript *o* denotes the actual value in the synthetic image.

$(\sigma_{PSF}/r_{eff})_o$	$\beta_0 = 0.25$	$\beta_0 = 0.50$	$\beta_0 = 1.00$
seeing ignored in the fit	$\beta$	$\beta$	$\beta$
0.05	0.2825	0.5136	1.005
0.10	0.3371	0.5448	1.019
0.25	0.4832	0.6638	1.102
0.50	0.7095	0.8842	1.299
0.75	0.9382	1.112	1.501
1.00	1.160	1.330	1.669
seeing underestimated by 10%	$\beta$	$\beta$	$\beta$
0.05	0.2539	0.5020	1.001
0.10	0.2594	0.5060	1.003
0.25	0.2769	0.5220	1.017
0.50	0.3108	0.5577	1.055
0.75	0.3528	0.6037	1.108
1.00	0.4063	0.6625	1.177
seeing overestimated by 10%	$\beta$	$\beta$	$\beta$
0.05	0.2463	0.4980	0.9990
0.10	0.2410	0.4940	0.9963
0.25	0.2237	0.4777	0.9815
0.50	0.1981	0.4408	0.9397
0.75	0.1914	0.3907	0.8747
1.00	0.1914	0.3318	0.7766

**Table 6.** Bulge/disk and bulge/disk/bar decompositions for 3 synthetic images. The values in parentheses are deviations from the correct values.

	weight	bulge/disk $B/D$ (dev)	$\beta$ (dev)	bulge/disk/bar $B/D$ (dev)	$\beta$ (dev)
model 1: $B/D=1.0$ , $\beta=0.5$ , $q=1.0$					
	1/F	0.97 (3 %)	0.50 (0 %)	1.23 (23 %)	0.59 (18 %)
	r	0.98 (2 %)	0.50 (0 %)	1.66 (66 %)	0.52 (4 %)
	constant	0.97 (3 %)	0.50 (0 %)	2.37	0.46 (8 %)
model 2: $B/D=0.92$ , $\beta=0.5$ , $q=0.9$					
	1/ F	0.87 (5 %)	0.50 (0 %)	1.13 (22 %)	0.60(20 %)
	r	0.88 (4 %)	0.50 (0 %)	1.50 (63 %)	0.52(4 %)
	constant	0.88 (4 %)	0.50 (0 %)	-	-
model 3: $B/D=1.0$ , $\beta=0.33$ , $q=1.0$					
	1/F	1.00 (0 %)	0.33 (0 %)	0.81 (19 %)	0.53 (60 %)
	r	1.00 (0 %)	0.33 (0 %)	0.98 (2 %)	0.50 (51 %)
	constant	1.00 (0 %)	0.33 (0 %)	20.80	0.28 (15 %)

**Table 7.** The decomposition results. The parameter B(all)/T in the last column indicates the B/T-ratio, when the fluxes of bars and ovals are included to the flux of the bulge.

NGC	Bulge $\beta$	$r_{eff} [^{\circ}]$	q	Disk $h_r [^{\circ}]$	(BBA) $h_r [^{\circ}]$	Ferr 1 $a [^{\circ}]$	q	Ferr 2 $a [^{\circ}]$	q	Ferr 3 $a [^{\circ}]$	q	B/T	B(all)/T
718	0.69	2.25	0.8	21.9	24.0	33.5	0.5					0.21	0.34
936	0.68	3.14	0.9	36.9	23.8	74.6	0.3	26.2	0.9			0.12	0.33
1022	0.46	1.41	0.9	19.8	19.5	32.6	0.4	12.7	0.6			0.10	0.29
1400	0.39	6.38	0.9	18.7								0.52	0.52
1415	0.63	1.67	0.6		21.5								
1440	0.71	2.33	0.8	20.4	19.9	35.8	0.3	16.0	0.9			0.14	0.33
1452	0.81	2.88	0.9	32.8	24.7	60.0	0.2	24.7	0.9			0.14	0.36
2196	0.36	9.28	0.8	24.1	27.2							0.45	0.44
2273	0.55	2.64	0.6	25.0		52.3	0.2					0.23	0.41
2460	0.39	4.69	0.8	10.5				20.5	0.4			0.27	0.29
2681	0.46	1.82	0.9	33.3	31.0	30.0	0.7	64.4	0.7	12.6	0.8	0.24	0.45
2781	0.35	4.36	0.8	54.7		52.2	0.9	14.2	1.0			0.29	0.65
2855	0.35	12.95	0.8	32.2								0.57	0.57
2859	0.77	4.65	0.9	78.2	18.8	79.6	0.4	10.2	0.6	73.4	1.0	0.27	0.54
2911	0.32	6.99	0.8	41.6	19.2							0.34	0.33
2983	0.76	1.70	0.8	27.6		47.9	0.3	17.9	1.0			0.11	0.35
3626	0.52	2.63	0.7	24.6	19.4	44.3	0.5					0.25	0.38
3941	0.67	2.52	0.9	21.8	20.1	35.4	0.6	16.4	0.9			0.17	0.35
4245	0.75	4.24	1.0	25.9	27.6	68.5	0.2	9.1	0.7			0.20	0.29
4340	0.54	4.44	1.0	41.1	10.9	131.0	0.1	36.9	0.5	11.3	0.7	0.32	0.48
4596	0.71	2.78	1.1	37.5	33.9	93.0	0.3	38.4	0.8			0.13	0.35
4608	0.72	3.29	0.9	36.7	34.1	62.4	0.3	24.9	0.9			0.15	0.40
4643	0.95	3.06	0.9	30.6	38.2	68.8	0.2	35.8	0.8			0.17	0.48

**Table 8.** Mean B/T-ratios.

	$B/T/(N)$ (S0)	$B/T/(N)$ S0/a+Sa	filter	bulge model
Burstein (1979)	$0.49 \pm 0.14$ (11)		<i>B</i>	$R^{1/4}$
Kent (1985)	$0.68 \pm 0.18$ (14)	$0.48 \pm 0.25(15)$	<i>R</i>	$R^{1/4}$
Simien (1986)	$0.57$ (31)	$0.41(5)$	<i>B</i>	$R^{1/4}$
APB95 (1995)	$0.32 \pm 0.13$ ( 7)	$0.20 \pm 0.13(7)$	<i>K</i>	Sérsic
SGA04 (2004)	$0.63 \pm 0.05$ (16)		<i>R</i>	Sérsic
CZ (2004)	0.45		<i>R</i>	$R^{1/4}$
This study	$0.24 \pm 0.11$ (14)	$0.28 \pm 0.14(9)$	<i>K</i>	Sérsic

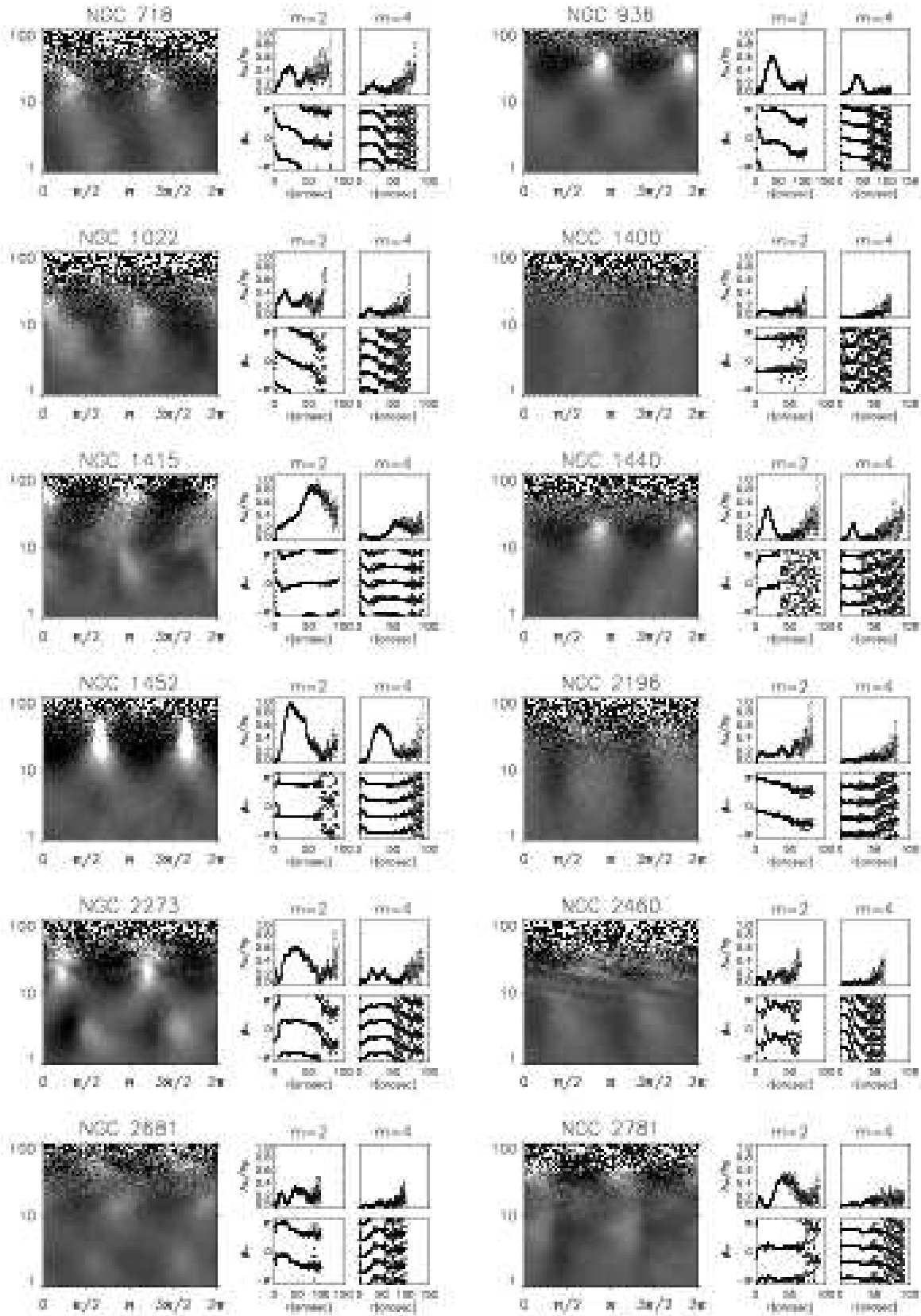


Fig. 1a

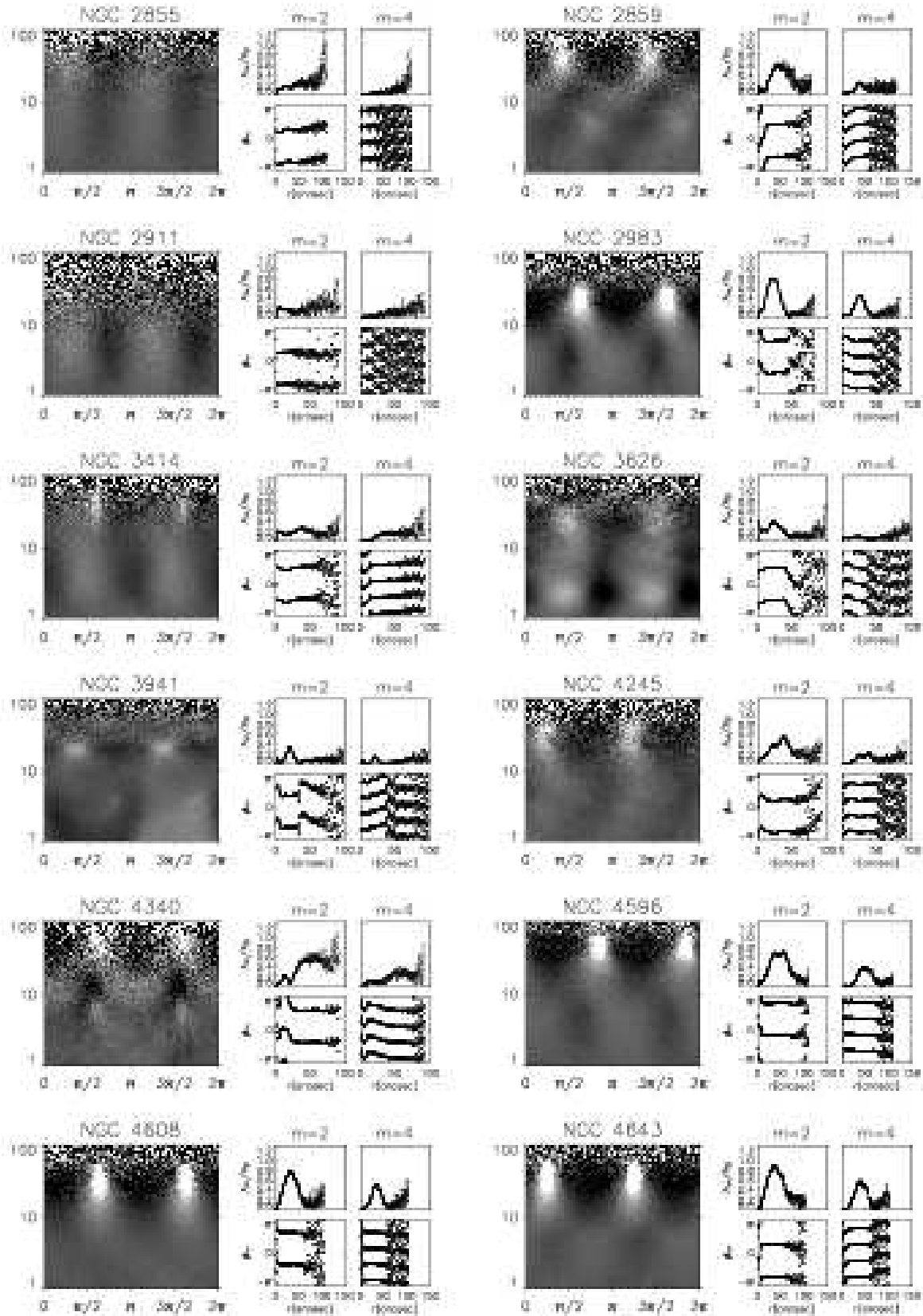


Fig. 1b



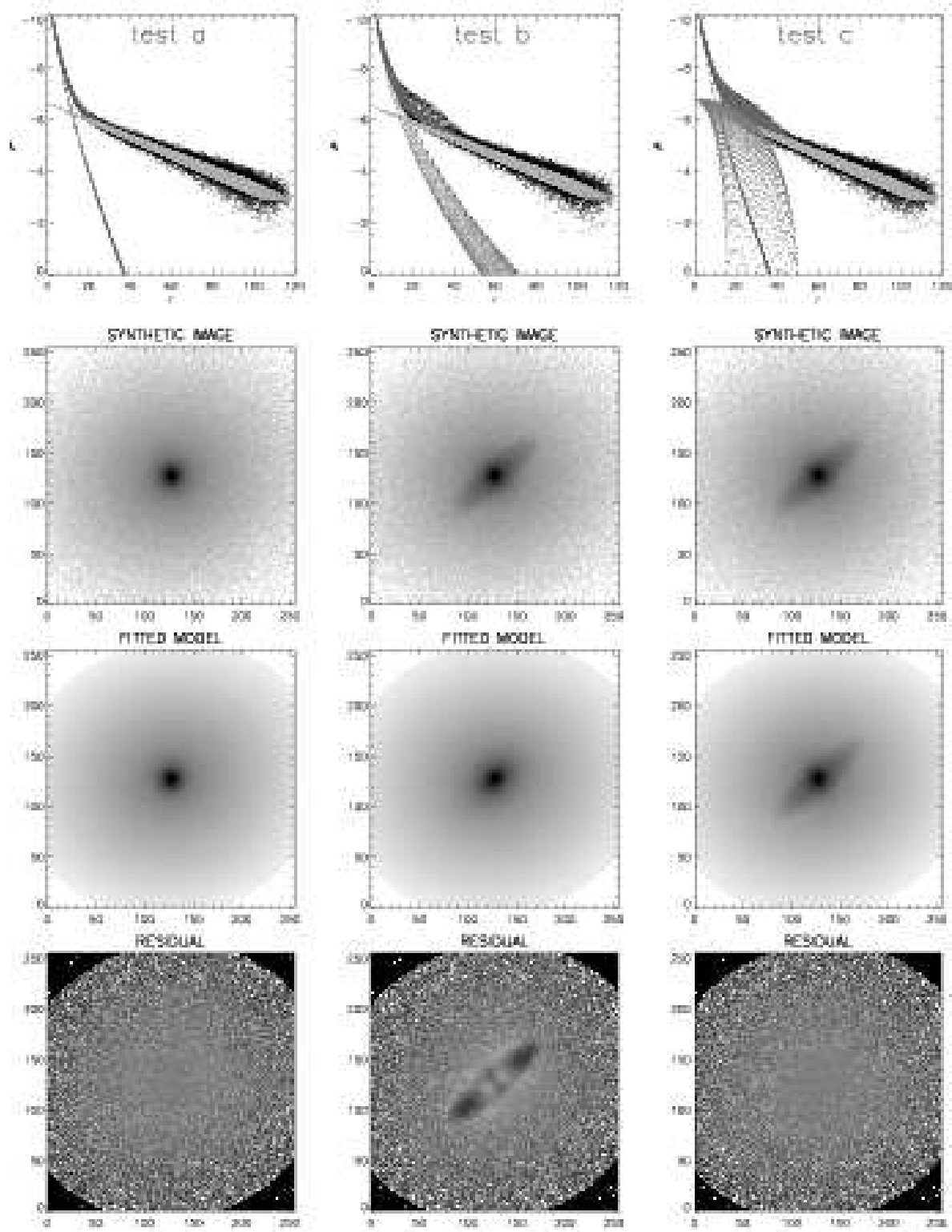


Fig. 2

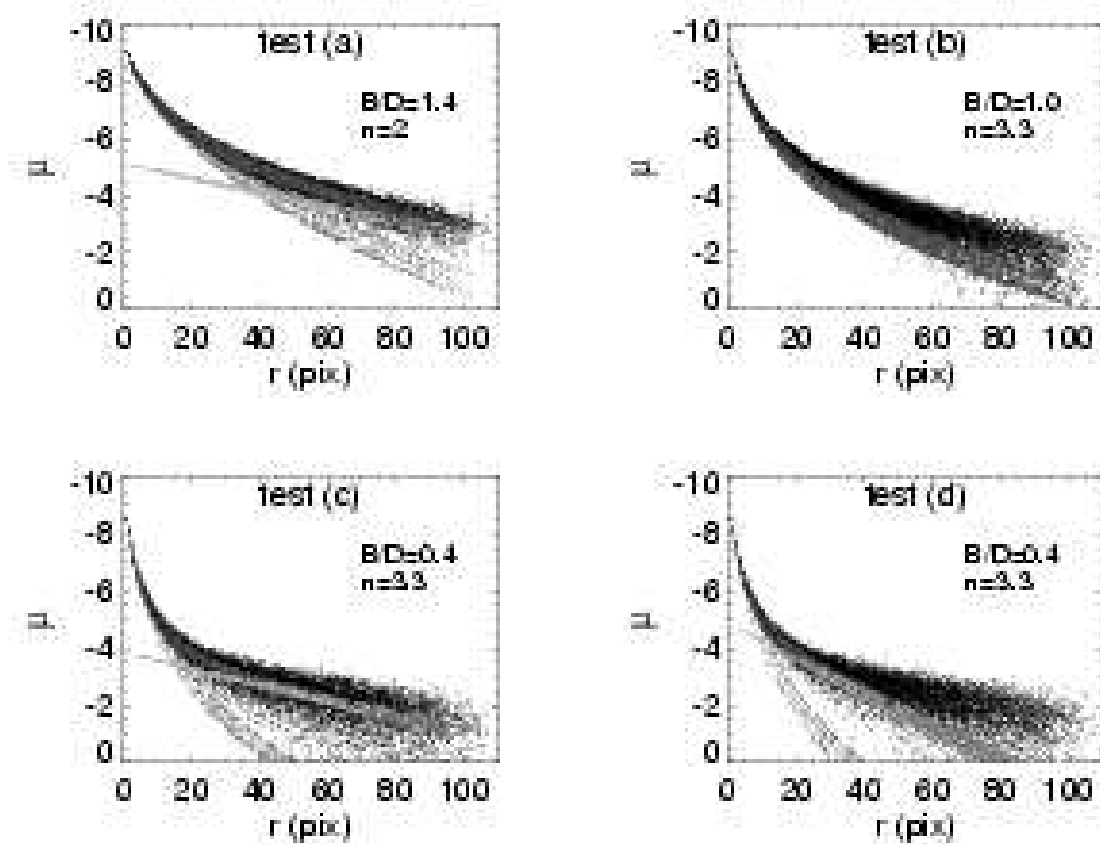


Fig. 3

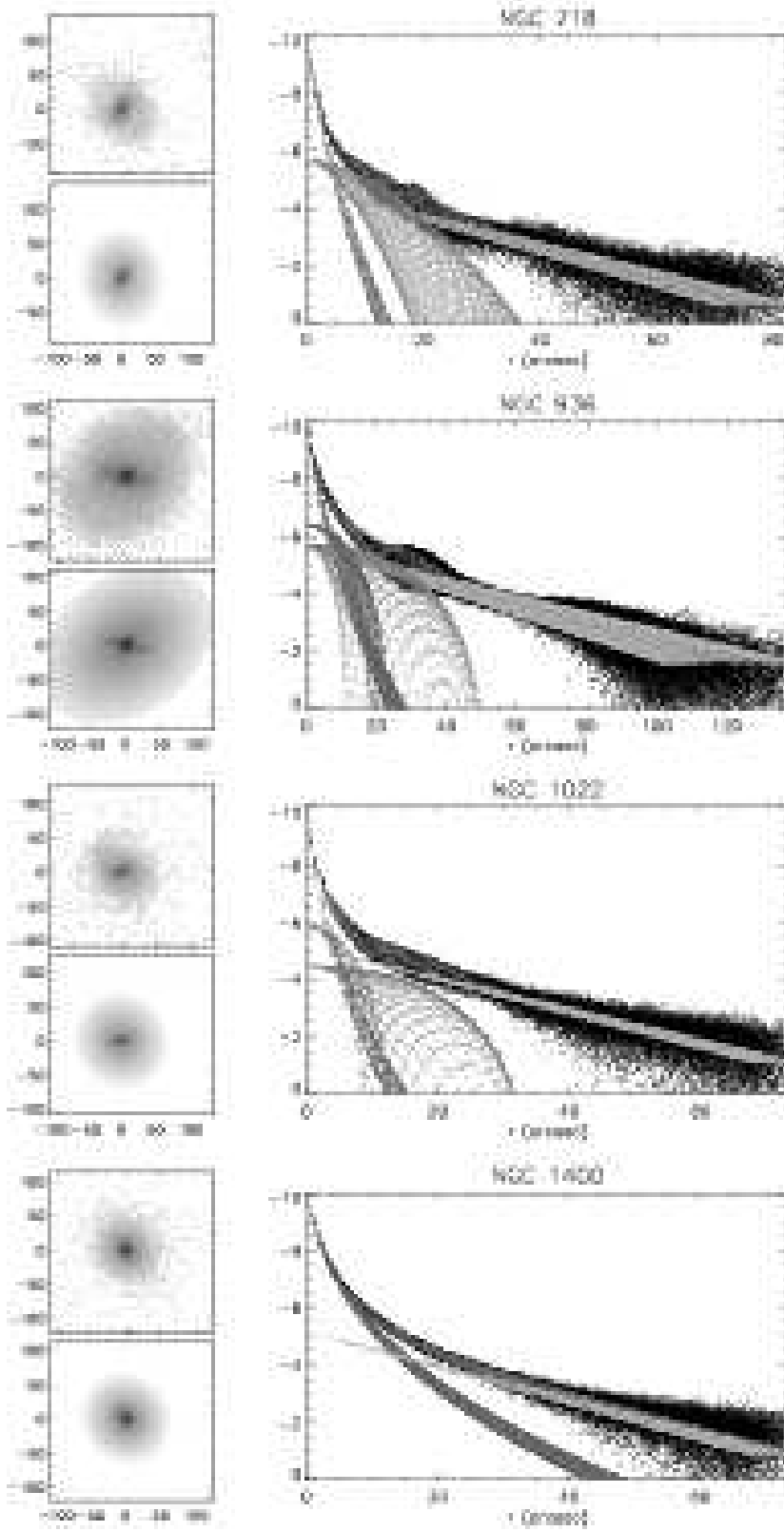


Fig. 4a

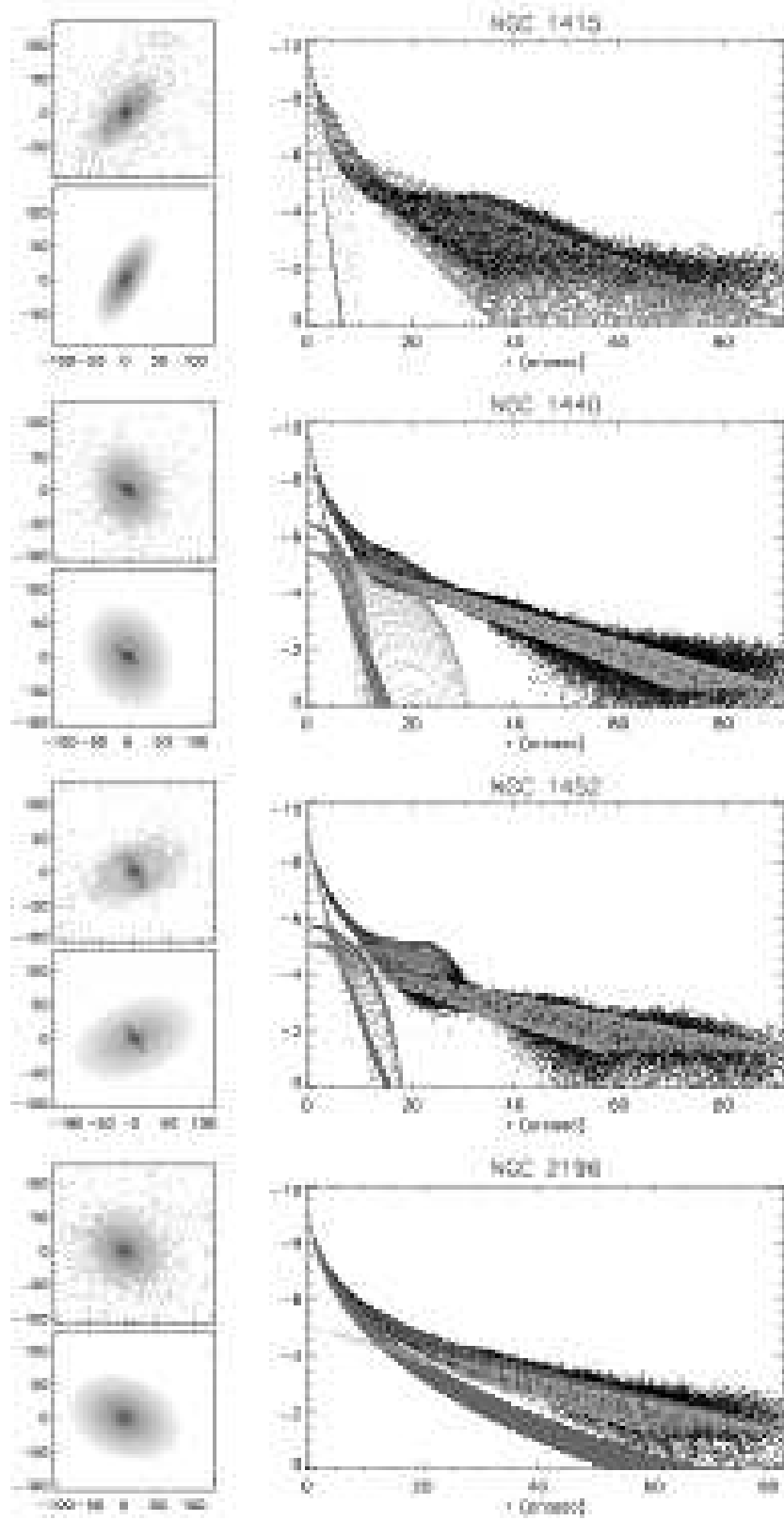


Fig. 4b

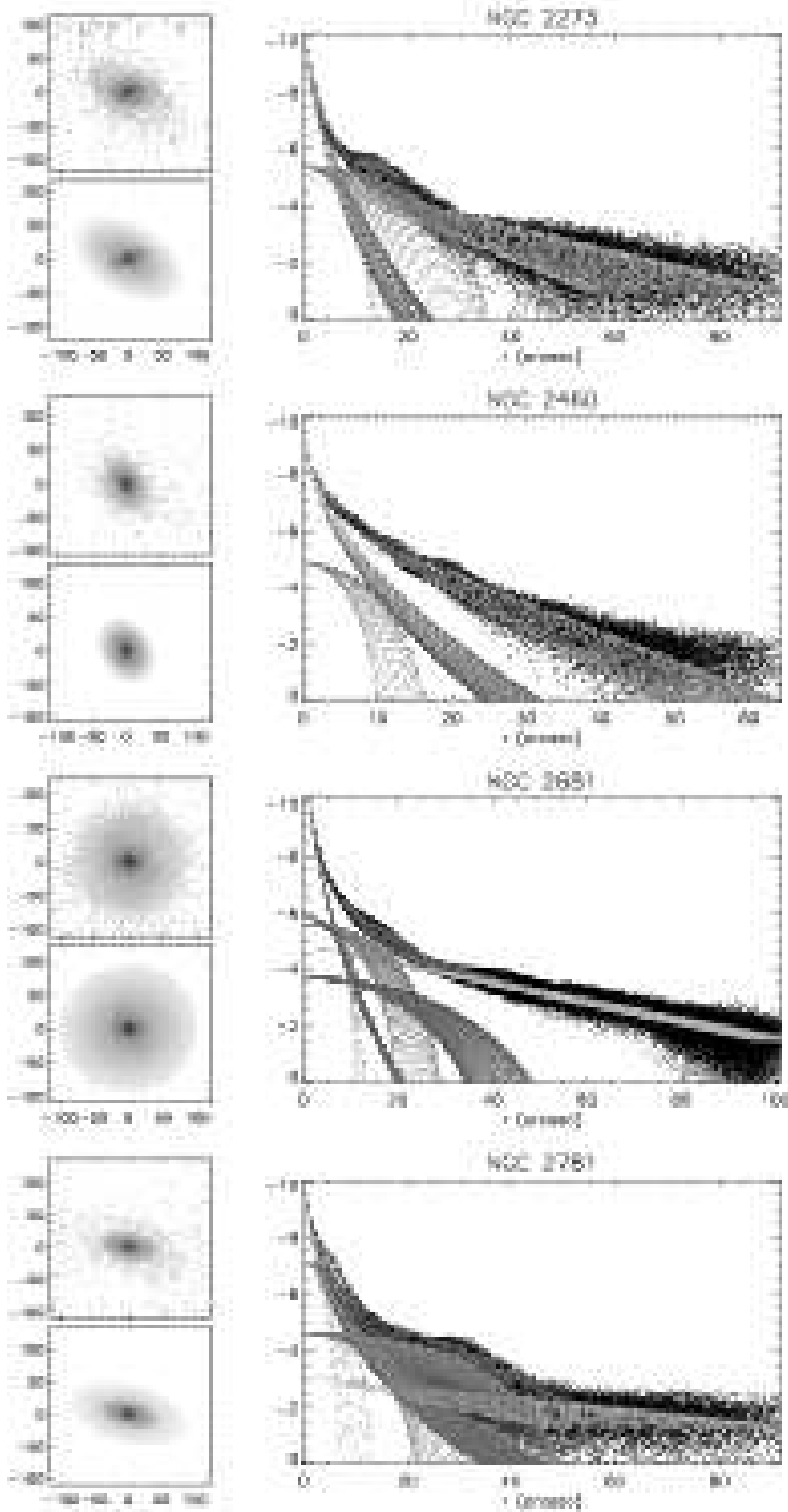


Fig. 4c

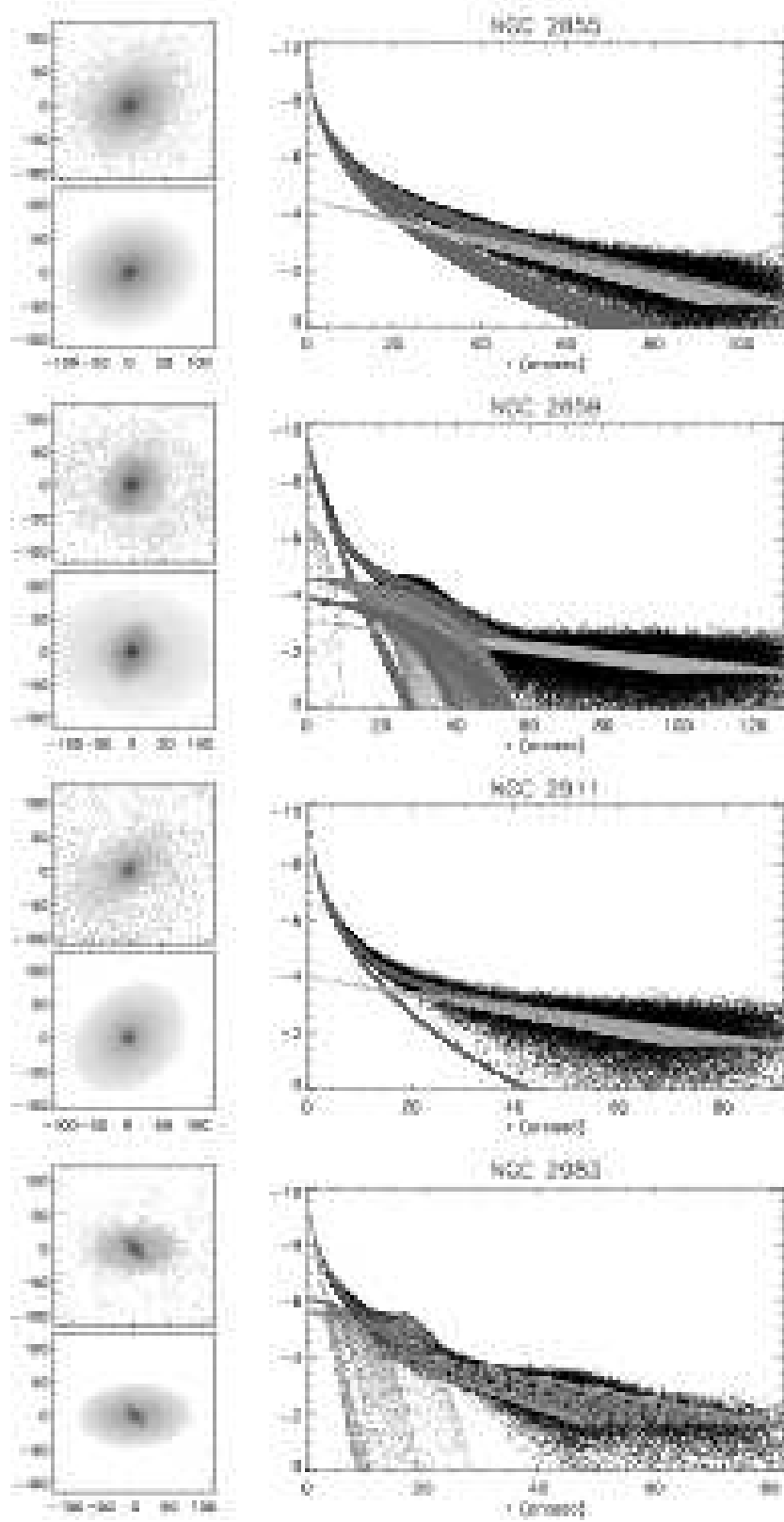


Fig. 4d

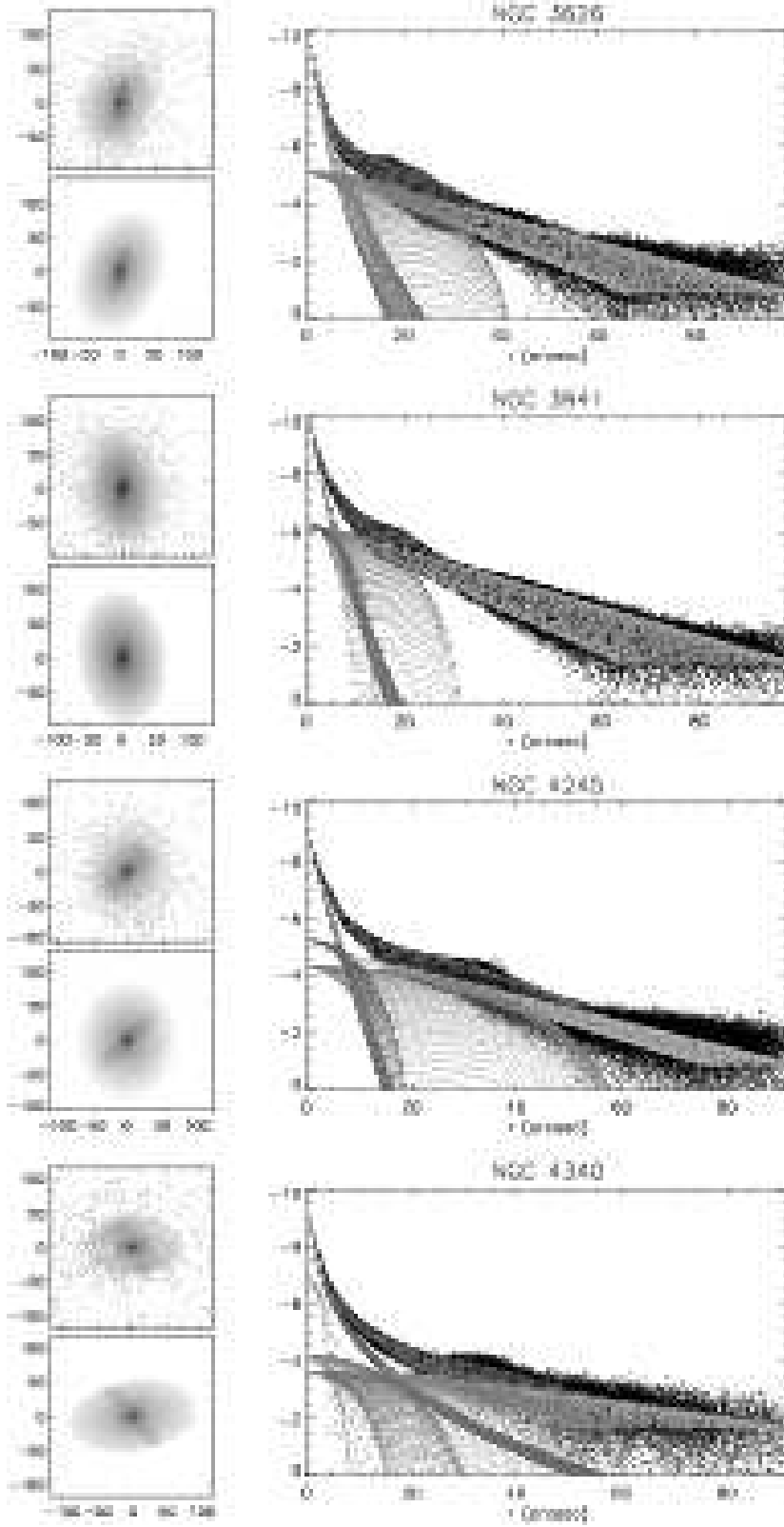


Fig. 4e

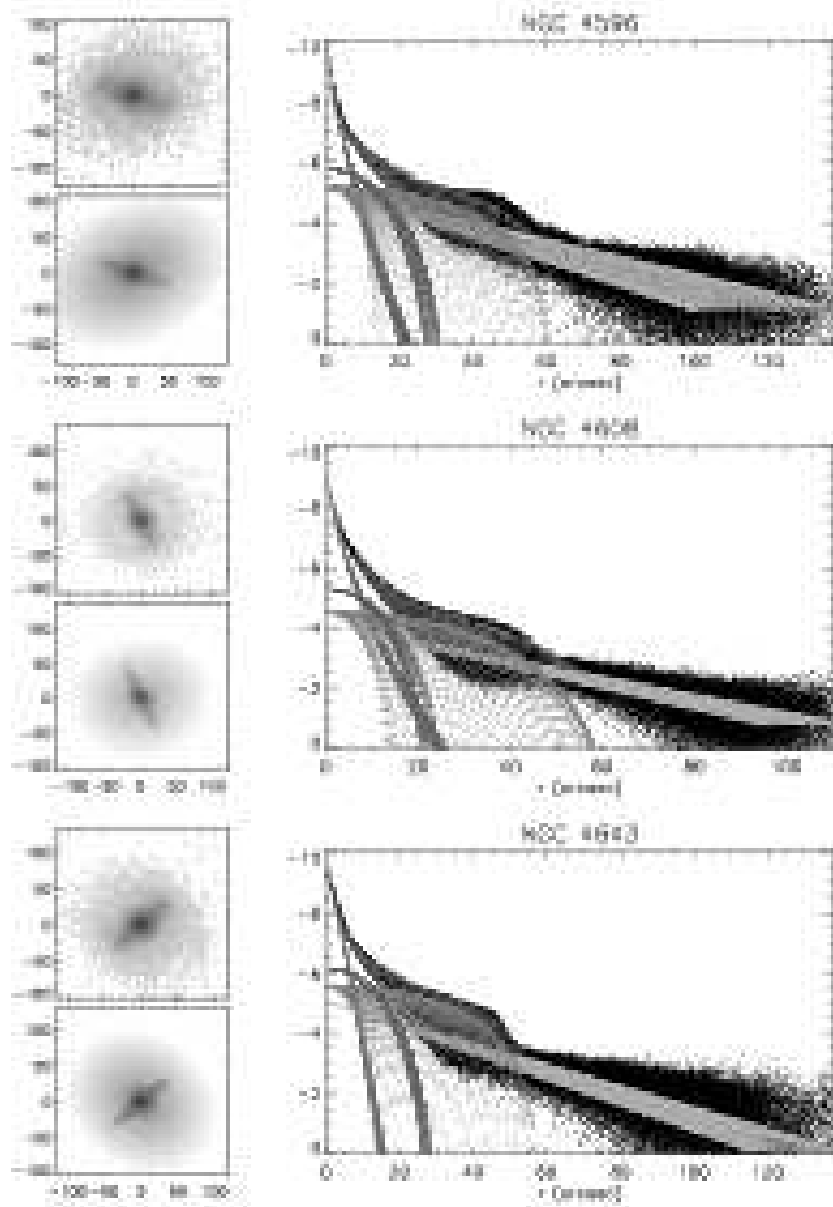


Fig. 4f



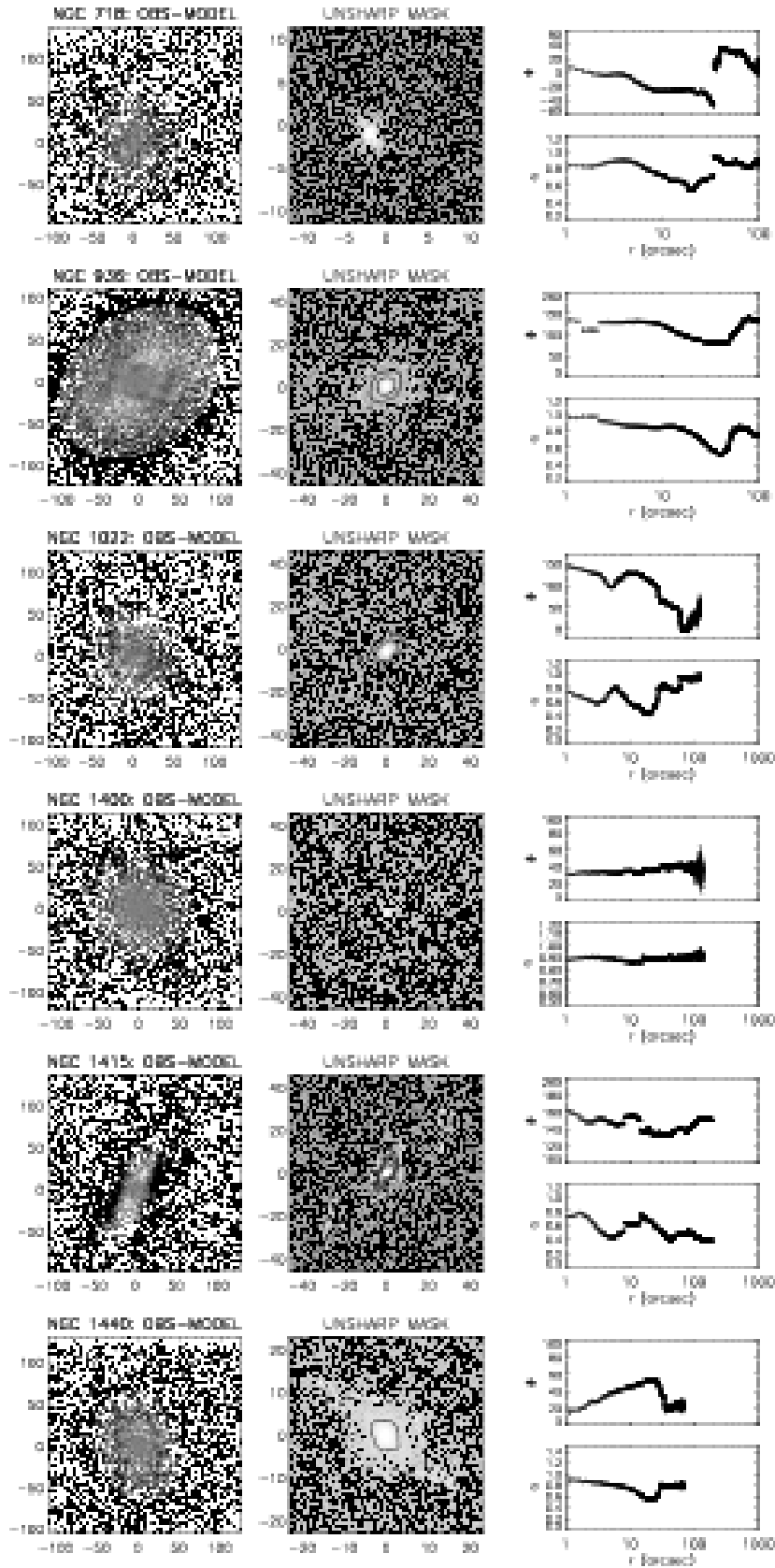


Fig. 5a

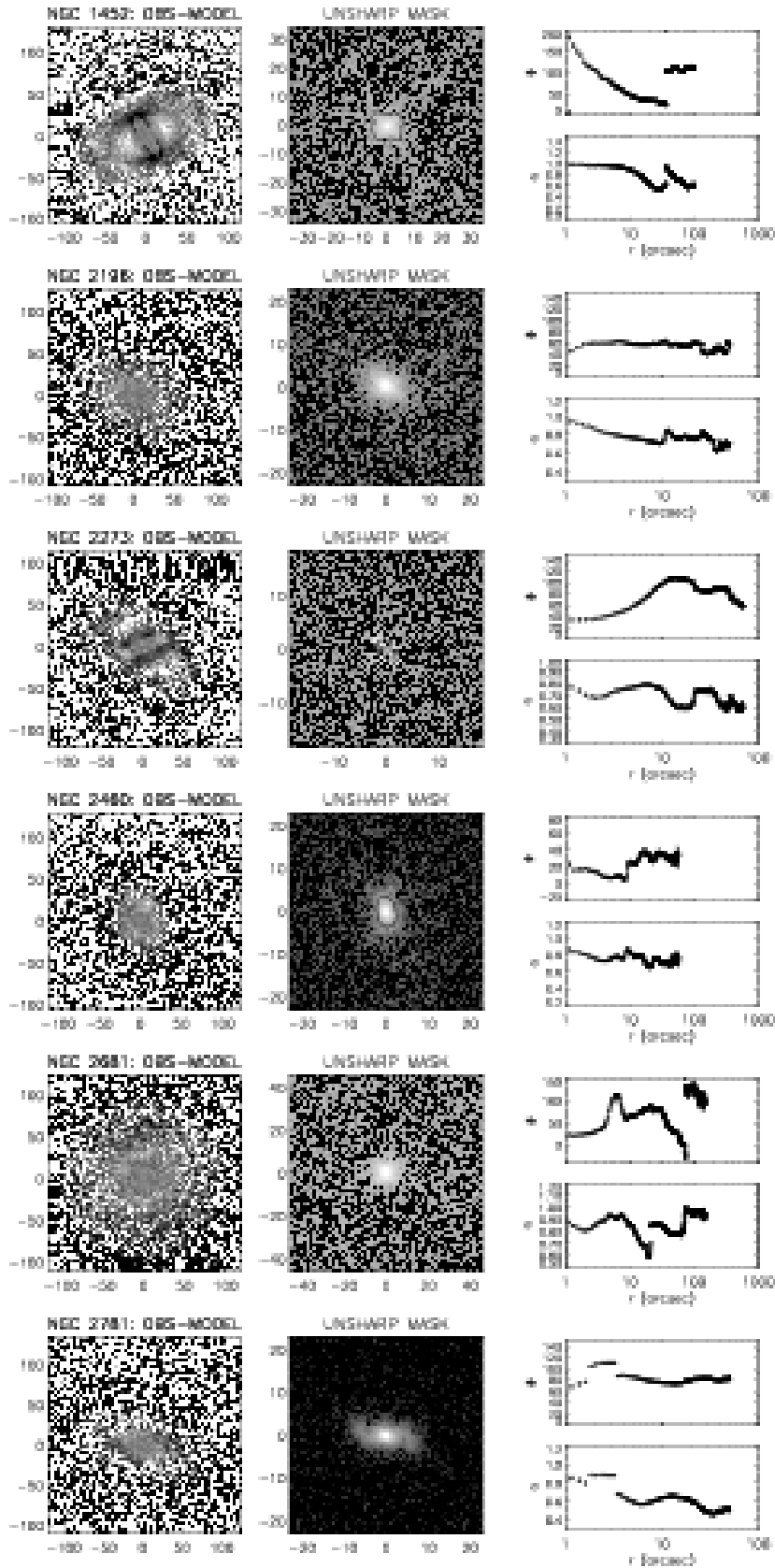


Fig. 5b

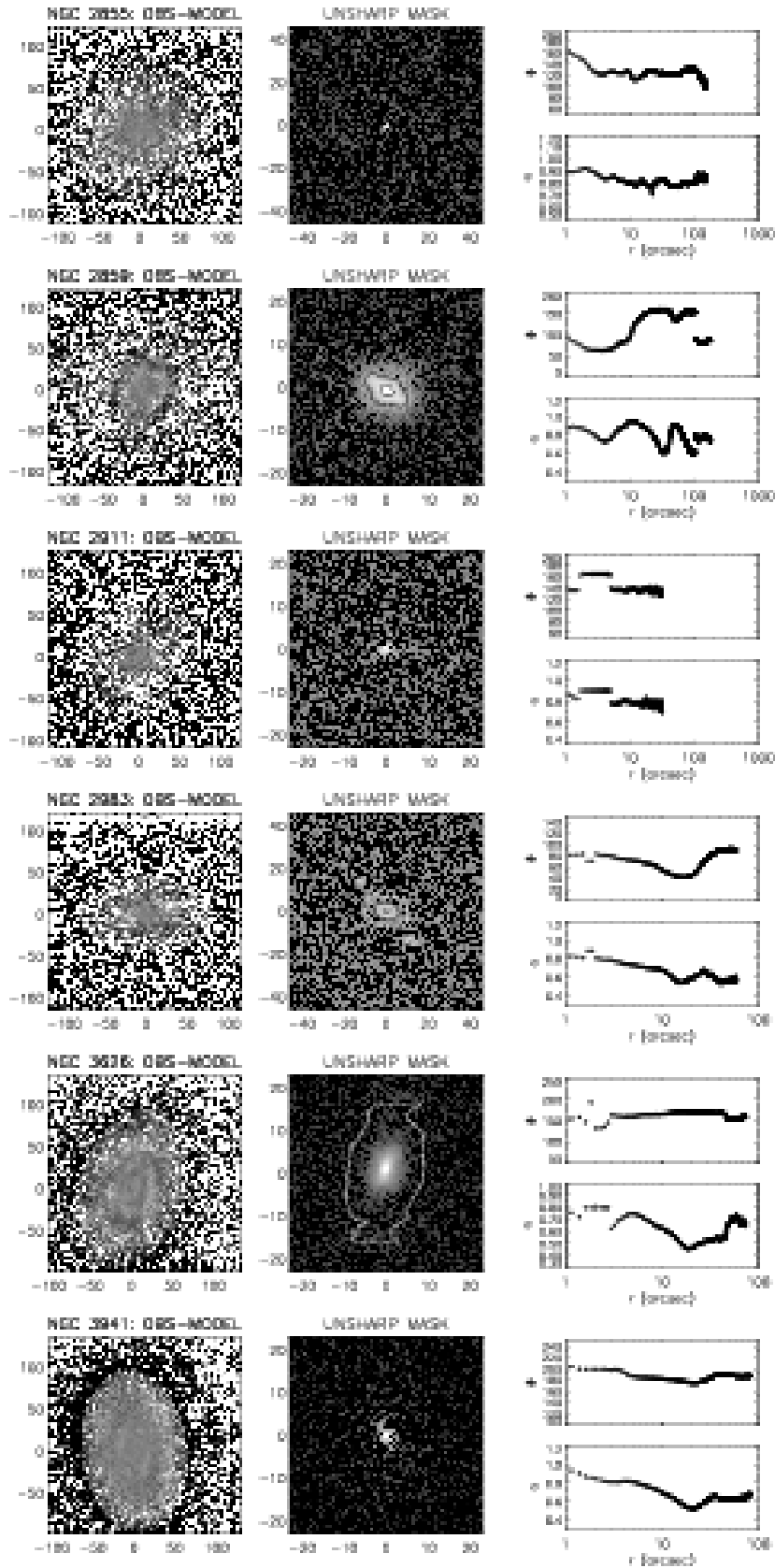


Fig. 5c

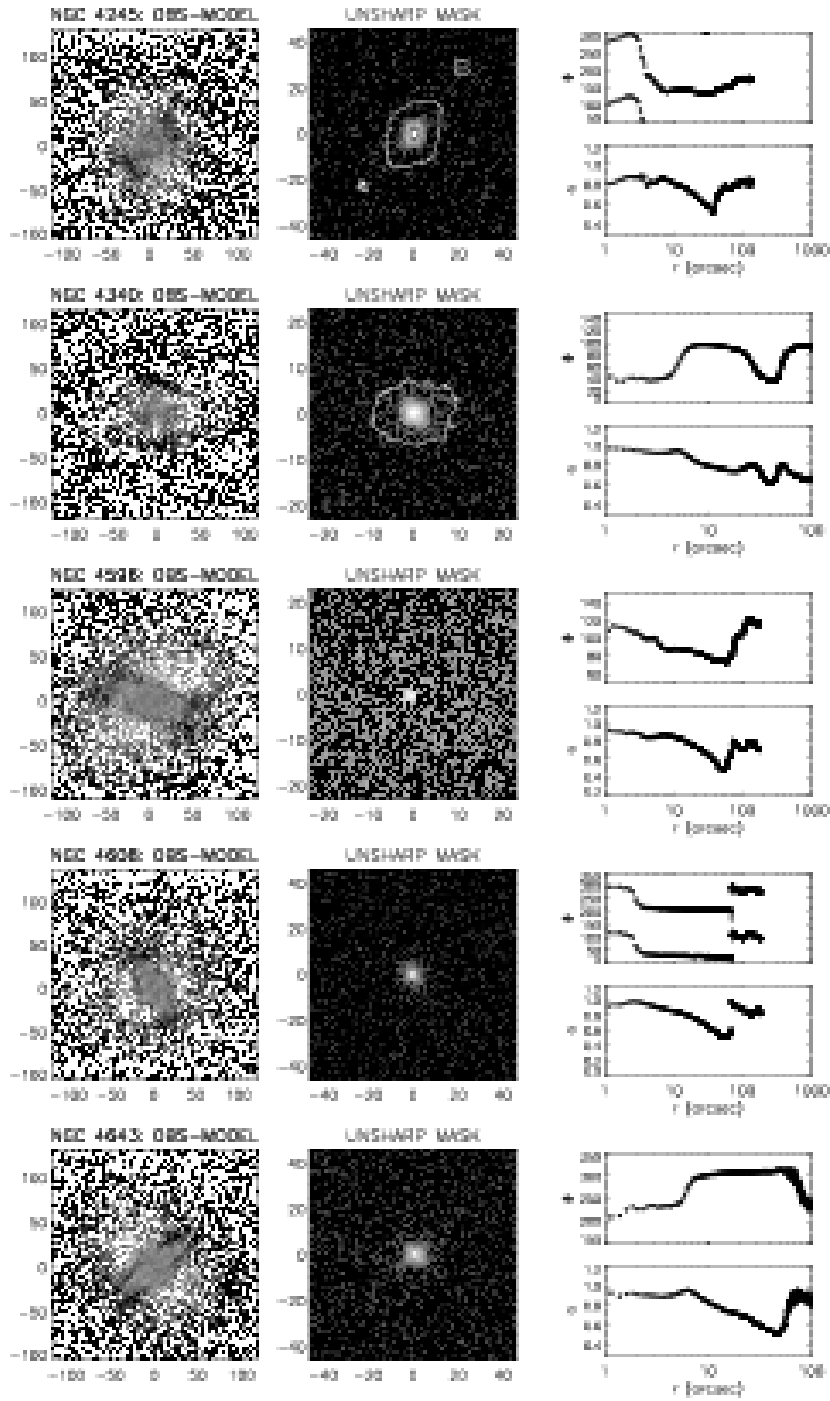


Fig. 5d

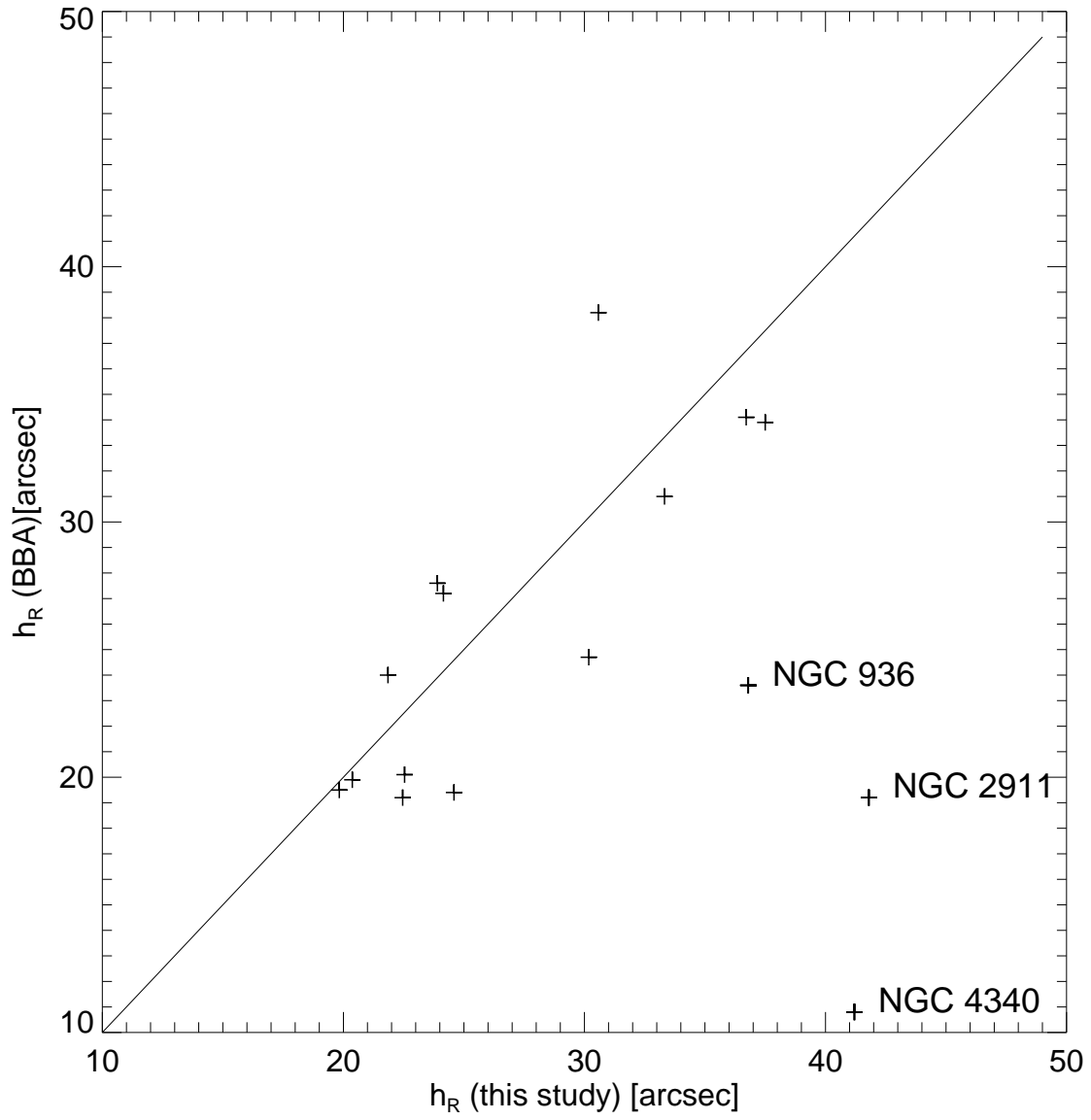


Fig. 6

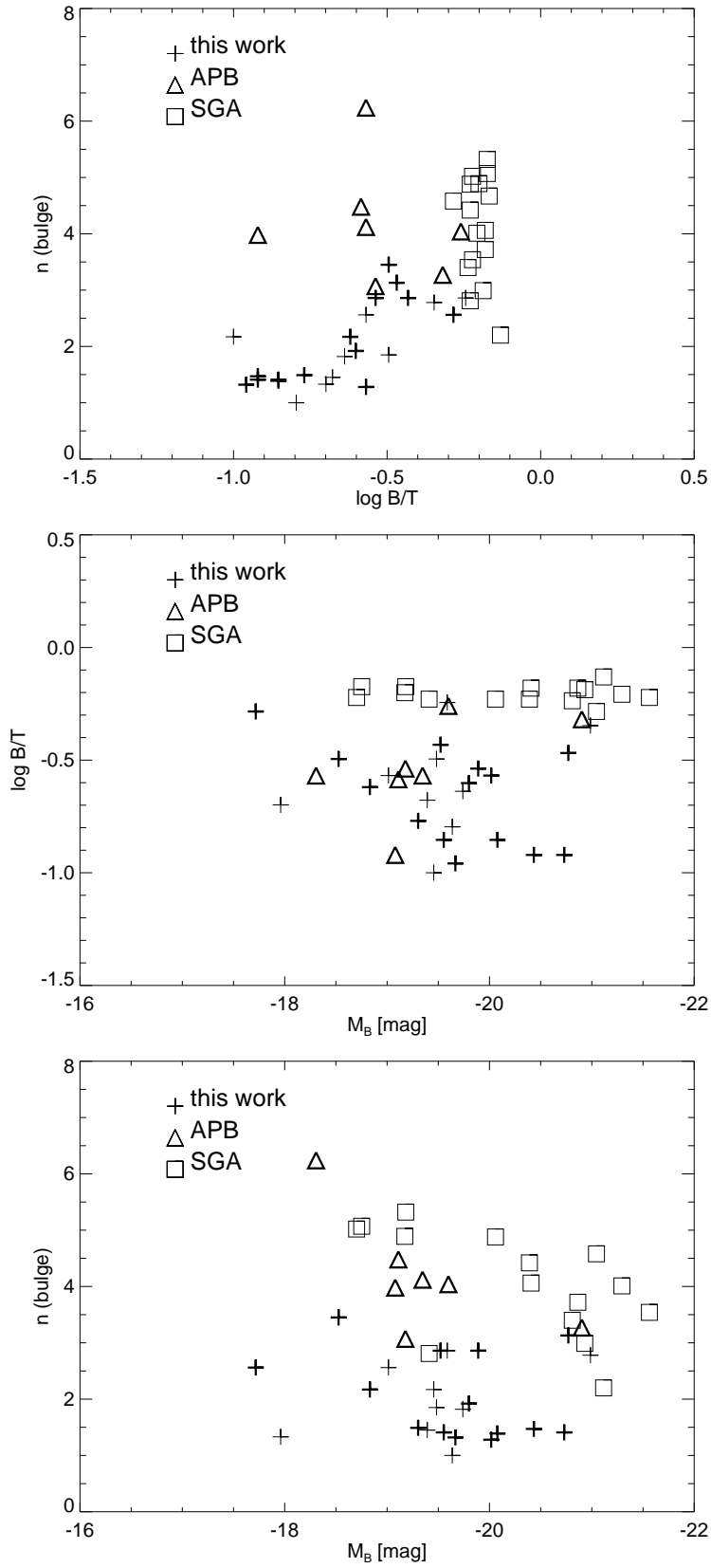


Fig. 7

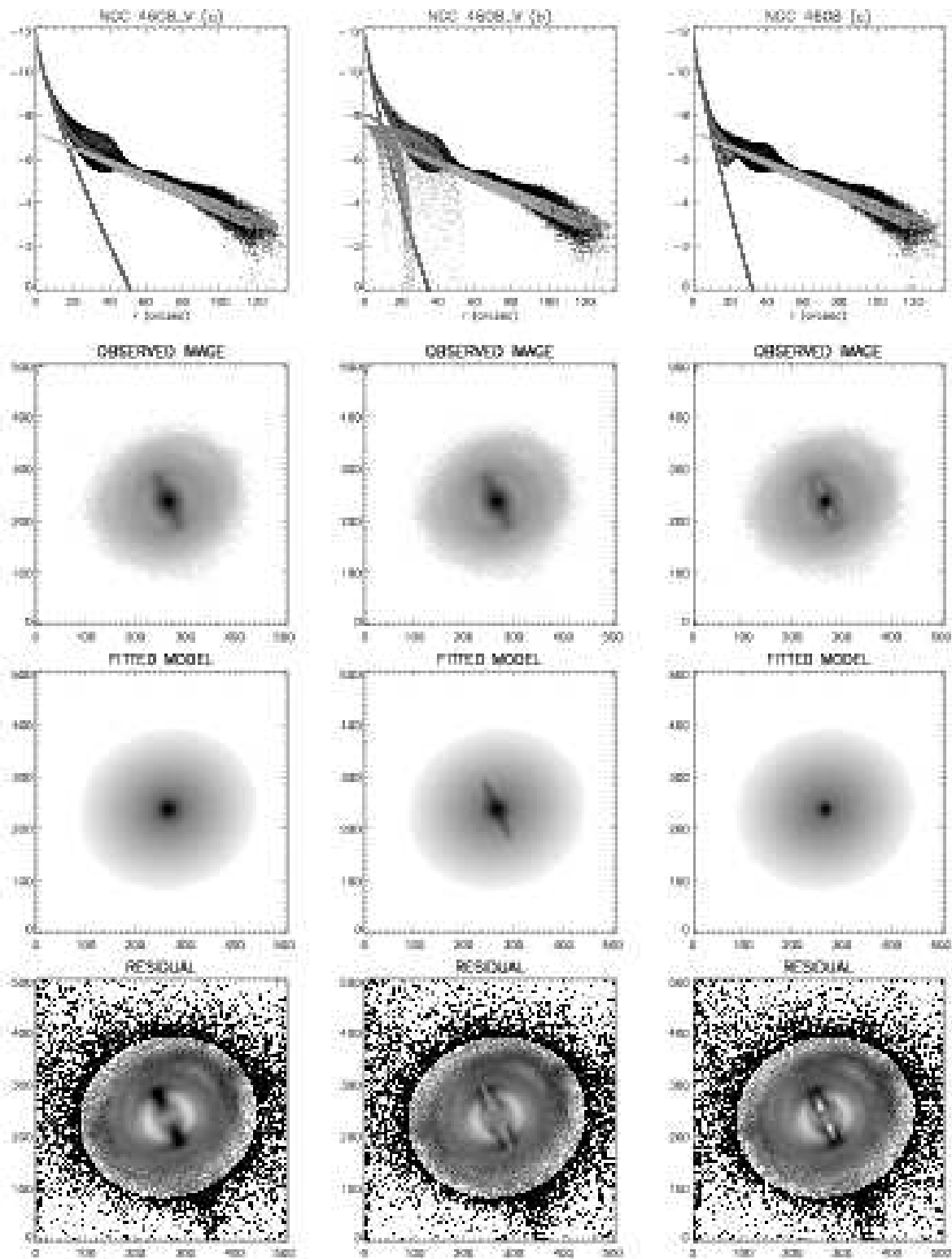


Fig. 8

This paper has been produced using the Royal Astronomical Society/Blackwell Science T<sub>E</sub>X macros.